

GEOTHERMAL RESOURCES IN SOUTHWESTERN UTAH: GRAVITY AND MAGNETOTELLURIC INVESTIGATIONS

by

Christian Lynn Hardwick

A thesis submitted to the faculty of
The University of Utah
in partial fulfillment of the requirements for the degree of

Master of Science

in

Geophysics

Department of Geology and Geophysics

The University of Utah

August 2013

Copyright © Christian Lynn Hardwick 2013

All Rights Reserved

THE UNIVERSITY OF UTAH GRADUATE SCHOOL

STATEMENT OF THESIS APPROVAL

The thesis of _____ Christian Lynn Hardwick _____

has been approved by the following supervisory committee members:

_____ David S. Chapman _____, Chair _____ 6/11/2013 _____

_____ Michael S. Thorne _____, Member _____ 6/14/2013 _____

_____ Richard G. Allis _____, Member _____ 6/13/2013 _____

and by _____ D. Kip Solomon _____, Chair of

the Department of _____ Geology and Geophysics _____

and by Donna M. White, Interim Dean of The Graduate School.

ABSTRACT

Recent geothermal studies on sedimentary basins in Western Utah suggest the possibility of significant geothermal reservoirs at depths of 3 to 5 km. This research focuses on 3 areas (Crater Bench, Pavant Butte, and Thermo), located within sedimentary basins having high geothermal potential. New geophysical data which include 364 gravity stations and 247 magnetotelluric (MT) stations collected during the summers of 2010 to 2012 have been used to augment historical gravity, electromagnetic, and borehole data where coverage is poor or insufficient. Two-dimensional gravity and MT models were created for these study areas in order to gain insight on the subsurface structural controls and to understand better the geothermal systems and potential of each study area. At Crater Bench, gravity and MT models show overall basalt flow thicknesses of 60 to 160 m and inferred depth-to-basement estimates of 1.3 to 3.6 km and a buried horst structure which is interpreted to be the structural control of the hot springs fluid flow. In the Pavant Butte study area, gravity and MT models display an elongate, mostly two-dimensional basin with a corridor about 15 km wide having 2 km of sediments on top of basement rock and in some areas reaching depths up to 3 km. Deep conductive bodies observed in this area hint at the presence of hot, saline fluids throughout the basin. Thermo displays intersecting gravity low trends of 4 to 10 mGal amplitude which intersect adjacent to the surface manifestation of the hot spring system and are interpreted as the structural control. Gravity and MT models indicate shallow depth-to-basement values (200 m) near the hot springs and up to 2 km to the southwest accompanied by low resistivities. Geothermal waters are old; water chemistry supports the conceptual model of waters migrating from the southwest basin up deeply penetrating faults and fractures to produce the hot springs. This geophysically-based study has added to the understanding of these potential geothermal systems.

CONTENTS

ABSTRACT	iii
LIST OF FIGURES	vi
ACKNOWLEDGEMENTS	vii
CHAPTERS	
1. INTRODUCTION	1
2. GEOPHYSICAL METHODS	4
2.1 Introduction to the Gravity Method	4
2.2 Introduction to the Magnetotelluric Method	9
3. CRATER BENCH	15
3.1 Introduction	15
3.2 Gravity	16
3.2.1 Survey and Modeling	16
3.2.2 Results	16
3.3 Magnetotellurics	17
3.3.1 Survey and Modeling	17
3.3.2 Results	18
3.3.3 Thickness of Basalt Flows	18
3.4 Discussion	19
4. PAVANT BUTTE	30
4.1 Introduction	30
4.2 Gravity	31
4.2.1 Survey and Modeling	31
4.2.2 Results	31
4.3 Magnetotellurics	32
4.3.1 Survey and Modeling	32
4.3.2 Results	33
4.4 Discussion	33
5. THERMO HOT SPRINGS	45
5.1 Introduction	45
5.2 Gravity	45
5.2.1 Survey and Modeling	45

5.2.2 Results.....	46
5.3 Magnetotellurics	47
5.3.1 Survey and Analysis	47
5.4 Discussion	48
6. SUMMARY AND CONCLUSIONS	54
REFERENCES	56

LIST OF FIGURES

1.1	Location map of study areas	3
2.1	Graphical representation of the phase tensor	14
3.1	Map of Crater Bench study area	20
3.2	Crater Bench CBGA map	21
3.3	Crater Bench 2D gravity model	22
3.4	Crater Bench MT survey map	23
3.5	Crater Bench phase tensor maps	24
3.6	Crater Bench geoelectric strike plot	25
3.7	Crater Bench phase tensor profile	26
3.8	Crater Bench dimensionality plot	27
3.9	Crater Bench 2D MT profiles	28
3.10	Crater Bench basalt thickness	29
4.1	Pavant Butte area map	35
4.2	Pavant Butte temperature plot	36
4.3	Pavant Butte CBGA map	37
4.4	Pavant Butte 2D gravity model	38
4.5	Pavant Butte MT survey map	39
4.6	Pavant Butte phase tensor maps	40
4.7	Pavant Butte geoelectric strike plot	41
4.8	Pavant Butte phase tensor profiles	42
4.9	Pavant Butte dimensionality plot	43
4.10	Pavant Butte 2D MT models	44
5.1	Thermo area map	49
5.2	Thermo CBGA map	50
5.3	Thermo 2D gravity model transect EF	51
5.4	Thermo 2D gravity model transect GH	51
5.5	Thermo MT survey map	52
5.6	Thermo phase tensor map	53

ACKNOWLEDGEMENTS

I would like to express my deepest appreciation to all those who provided me the possibility to complete this research. I would like to thank my thesis advisor, David S. Chapman, for taking me under his wing and introducing me to geothermal geophysics along with the guidance, useful comments, and engagement through the learning process of this masters thesis. I also want to express thanks to my other committee members, Richard G. Allis and Michael S. Thorne, for their invaluable support and feedback. Furthermore, I want to thank the members of the Friends of Lord Kelvin and my thermal lab peers Mike Davis, Mason Edwards, Paul Gettings, Derrick Hasterok, Melissa Masbruch, and Imam Ruharjo for the meaningful discussions and constructive feedback they offered throughout this research. I would like to sincerely thank my lab colleague, Paul Gettings, for all the help he has given me from assisting in field work to the processing and interpretation of field data.

I am sincerely appreciative for financial assistance from ARRA funds, State Energy Program, and the Department of Geology and Geophysics of the University of Utah. I would also like to thank the staff of the Utah Geological Survey for field support, the use of their geophysical equipment, and the valuable comments and discussions related to this research. I also would like to thank Grant Caldwell, Graham Hill, George Jiracek, and Phil Wannamaker for all of their assistance in understanding electromagnetics and their unsolicited advice and insight regarding this research.

I would like to thank my loved ones, who have supported me throughout the entire process. Above all else, I would especially like to express my gratitude and praise of my wife, Robyn Hardwick, who has been by my side all those late nights and persevered through the times when I was away from home doing field work and research. I will be forever grateful for your love and support of my academic endeavors.

CHAPTER 1

INTRODUCTION

Several lines of geological and geophysical evidence point to a previously unrecognized geothermal resource beneath the deserts of central Utah. The Sevier Thermal Belt (Figure 1.1), which is the location of most of Utah's moderate and high-temperature ($>90^{\circ}\text{C}$) hydrothermal systems, is a north-south trending region that covers the edge of the Basin and Range province and the Basin and Range-Colorado Plateau transition zone [Blackett, 2007]. It is characterized by high regional heat flow (90 to 150 mW m^{-2}), zones of active seismicity, abundant Late Cenozoic normal faults, Tertiary volcanic and plutonic rocks, and Quaternary basalt and rhyolite [Blackett, 2007]. The Sevier Thermal Belt is inclusive of the Sevier, Black Rock, and Escalante Deserts. In a preliminary geothermal assessment of west-central Utah by Nash *et al.* [1978], they concluded that the Black Rock Desert contains the youngest basalt and rhyolite of the area including calculated water temperatures in excess of 200° and is an "attractive area for detailed exploration for concealed heat sources." There are several areas historically identified as Known Geothermal Resource Areas (KGRA) within the thermal belt though not all of them have been examined closely.

In this research, we focus on 3 such areas (Crater Bench, Pavant Butte, and Thermo Hot Springs), shown in Figure 1.1, in order to improve the understanding of these resource areas and determine their potential in regards to future development. Geophysical survey methods of gravity and magnetotellurics (MT) are employed to delineate subsurface controls, characterize the geothermal system, and help quantify the geothermal potential of each area. The gravity method is sensitive to the density contrasts of subsurface materials and attentive modeling of the data provides insight to buried structure geometries. The MT method is sensitive to the electrical properties of subsurface materials such as resistivity or conductivity and the modeling

of MT data provides insight to subsurface electrical characteristics and structure. The MT method has been applied extensively in geothermal settings due to the sensitivity of pore fluid electrical properties to temperature.

For areas of interest that are located in basin settings, these surface geophysical surveys are well suited to delineate subsurface structures. A multidisciplinary approach to obtain integrated solutions in Earth science problems, as discussed by *Saltus and Blakely* [2011], is practically a necessity in potential field studies in order to achieve effective results. Electrical surveys may be used to infer subsurface reservoir characteristics (for example, *Garg et al.* [2007]; *Johnston et al.* [1992]) and are useful in deep sedimentary basins as shown by, for example, *Bujakowski et al.* [2010] and *Wannamaker et al.* [2006].

A handful of geophysical surveys have been carried out in the above-mentioned areas of interest. A total of 364 gravity stations and 247 MT stations were added during the summers of 2010, 2011, and 2012. This new data significantly improved geophysical coverage, filling large gaps and spans in locations where previous surveys were hindered by limited access. To supplement the gravity survey and existing rock density data [*Crebs*, 1976; *Thangsuphanich*, 1976; *Sawer*, 1977; *Brumbaugh*, 1978; *Carter*, 1978], a total of 42 rock samples were collected from outcrops at various locations throughout the study areas to be measured for density values.

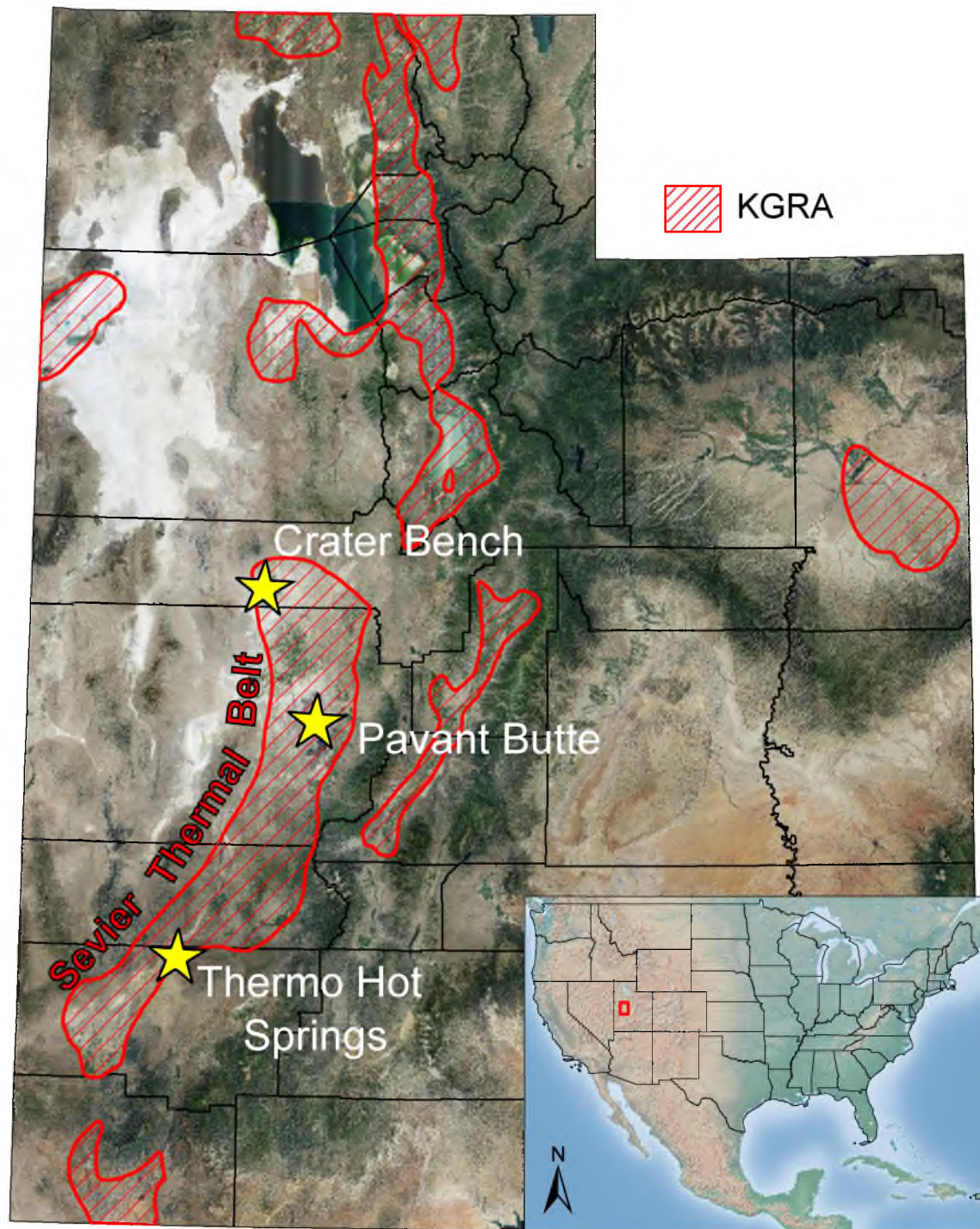


Figure 1.1. Location map of study areas. Known Geothermal Resource Areas (KGRA) are indicated by red hatched areas, solid black lines are county boundaries on the state map and are state boundaries on the U.S.A inset map. All 3 study areas, indicated by yellow stars, lie within the Sevier Thermal Belt of Utah.

CHAPTER 2

GEOPHYSICAL METHODS

2.1 Introduction to the Gravity Method

Natural density variations in the Earth's subsurface result in small variations of the Earth's gravitational field. By careful measurement of the gravity field, these small variations are quantified and we are able to infer density variations due to subsurface structure by modeling gravity anomalies (observed gravity – predicted gravity). Modern gravimetry instrumentation and techniques allow measurement of the gravitational field to about 1 part per billion (1 μGal). To put this into perspective, the mean value of the acceleration due to gravity at the Earth's surface, g , is 9.8 m s⁻² or 980 Gal (a working gravity unit equal to 1 cm s⁻²).

Gravity is also sensitive to distance from center of mass so an accurate elevation measurement is an important part of gravity surveys. The vertical gravity gradient is

$$\frac{\partial}{\partial r}g = \frac{\partial}{\partial r} \left(-\frac{GM_E}{r^2} \right) = \left(-\frac{2GM_E}{r^3} \right) = \left(-\frac{GM_E}{r^2} \right) * \left(\frac{2}{r} \right) = -\frac{2}{r}g, \quad (2.1)$$

where G is the gravitational constant, M_E and r are the mass and radius of the Earth, respectively. With values of $g = 981$ Gal and $r = 6357$ km,

$$\frac{\partial}{\partial r}g = -0.3086 \text{ mGal m}^{-1}. \quad (2.2)$$

Thus an elevation uncertainty of 1 m equates to an uncertainty of 0.3 mGal in observed gravity; an uncertainty of 1 cm equates to an uncertainty of 3 μGal . This is in addition to uncertainties due to instrument precision and error.

The horizontal gravity gradient can be shown conventionally, for example, by using the 1980 International Gravity Formula [Moritz, 1980]

$$g(\phi) = g_e(1 + a \sin^2 \phi - b \sin^2 2\phi) \quad (2.3)$$

where $g_e = 978032.67715$ mGal, $a = 0.0053024$, $b = 0.0000058$, and ϕ is latitude. The last term is small and can be ignored in this example. If we take the derivative w.r.t. latitude

$$\frac{\partial}{\partial \phi} g(\phi) = \frac{\partial}{\partial \phi} g_e(1 + a \sin^2 \phi) = g_e a(2 \cos \phi \sin \phi) = g_e a(\sin 2\phi) \text{ mGal rad}^{-1}. \quad (2.4)$$

When we substitute the values for g_e , a and convert units we have

$$\frac{\partial}{\partial \phi} g(\phi) = 0.815 \sin 2\phi \text{ mGal km}^{-1}. \quad (2.5)$$

The maximum gradient is at a latitude of 45° at 0.8 mGal km^{-1} . When compared to the vertical gradient, it is clear that inaccuracies in elevation measurements have much larger consequences (3 orders of magnitude) than those of the horizontal position.

The accuracy of gravimeter instrumentation and processing in ground surveys typically far exceed Global Positioning Systems (GPS) or other positioning equipment in measurement capabilities in the station time available, leaving the elevation accuracy as the limiting factor. It should be noted that in most cases, gravity measurements are made over a specified time as a time-series in order to mitigate transit effects on the meter or other time varying noise. However, gravimeters achieve suitable accuracies in a shorter amount of time than that required by GPS equipment (10 minutes vs. 4 to 8 hours). Consequently, the efficiency of gravity surveys is primarily determined by the elevation control needed. Higher accuracy requires a longer amount of time at each station which reduces the total amount of gravity stations established in a given campaign duration.

Station occupation times are scaled according to elevation and gravity accuracy requirements. In a regional gravity survey where anomalies are on the order of >20 mGal, an uncertainty of 0.1 mGal is acceptable. However, when high-precision gravity is required (as is the case of groundwater studies), an uncertainty of 0.1 mGal ($100 \mu\text{Gal}$) would lose the signal in the noise. Another consideration is the spatial coverage of existing gravity stations for your field area. By incorporating existing observations, assuming high-quality data, one decreases the amount of measurements needed to get acceptable coverage of the study area. By balancing the aforementioned

constraints in regards to your target, one can then maximize the efficiency and effectiveness of a gravity survey. Since the gravitational field can be easily measured at the Earth's surface without need to disturb the environment, the gravity method lends itself as a cost-effective, noninvasive, low-impact geophysical technique in subsurface studies.

The most common way to express and interpret gravity anomaly data is with the complete Bouguer gravity anomaly (CBGA). The CBGA shows the departure of observed gravity from the predicted gravity based on a crustal model of constant density. The anomaly incorporates theoretical gravity, free air, Bouguer, and terrain corrections. The CBGA in this study were computed using a reduction density of 2.67 g cm^{-3} (2670 kg m^{-3}) and the formulas, referenced to the WGS84 ellipsoid, outlined in the work of *Hinze et al.* [2005] are shown below. Gravity, g_T , on the surface of the best-fitting, rotating ellipsoid (GRS80) of the earth is given by

$$g_T = \frac{g_e(1 + k \sin^2 \phi)}{(1 - e^2 \sin^2 \phi)^{1/2}}, \quad (2.6)$$

where g_e , the normal gravity at the equator, is $978032.67715 \text{ mGal}$, $k = 0.001931851353$, e^2 is 0.0066943800229 , and ϕ is the latitude of the observation point. The gravity effect of the height of the observation point relative to the vertical datum of the reference ellipsoid, known as free-air correction, is given by

$$g_{FA} = -(0.3087691 - 0.000439 \sin^2 \phi)h + 7.2125 \times 10^{-8}h^2, \quad (2.7)$$

where h is height in meters and ϕ is latitude of observation point. The Bouguer slab corrections account for the gravitational attraction of the layer of earth between the ellipsoid and the observation point

$$g_{BC} = 2\pi\rho Gh = 4.193 \times 10^{-5}\rho h \quad (2.8)$$

where G , the gravitational constant, is $6.673 \times 10^{-11} \text{ m}^3 \text{ kg}^{-1} \text{ s}^{-2}$, ρ is density in kg m^{-3} , and h is height in meters. The above equation is representative of an infinite horizontal slab and a revised procedure recommends using a spherical cap of radius

166.7 km to account for the curvature of the Earth in place of the slab approximation [Hinze *et al.*, 2005]. The spherical cap correction is given by

$$g_{SC} = 2\pi\rho G(\mu h - \lambda R) \quad (2.9)$$

where μ and λ are dimensionless coefficients [LaFehr, 1991] and R is the radius of the Earth at the station. Terrain corrections account for gravity effects due to topography changes which can be considered as the departure from the assumed horizontal slab or spherical cap used in the Bouguer slab correction [Hammer, 1939]. Two zones were used for terrain corrections. First, from the station out to 68 m is the inner-zone terrain correction (IZTC). Second, from the edge of the inner-zone (68 m) out to 166.7 km is the outer-zone terrain correction (OZTC). Furthermore, terrain correction values are always positive since being on top of a hill or in a depression both result in the measured gravity being less than the Bouguer slab assumption. The total terrain correction, g_{TC} is given by

$$g_{TC} = g_{IZTC} + g_{OZTC}. \quad (2.10)$$

After computing the predicted gravity for the observation point, the equation for CBGA is

$$g_{CBGA} = g_{obs} - g_{pred} = g_{obs} - [g_T + g_{FA} + g_{BC} + g_{TC}], \quad (2.11)$$

where g_{obs} is the observed gravity value and g_{pred} is the predicted gravity. It should be noted that the CBGA does not remove regional gravity effects, such as crustal thickness variations. When modeling on a local scale, regional signals should be removed from the CBGA, leaving just the residual (local) values to be analyzed. To a first approximation, near-surface structure results in short-wavelength gravity anomalies and deeper structure results in long-wavelength gravity anomalies. This wavelength relationship is due to the inverse square relation of distance and gravity (i.e., larger gravity effects for smaller distances and vice versa). The regional gravity signal is a consequence of changes in deeper structure and can be approximated with a low-order polynomial in the 2D case or with a parametric surface in the 3D case. In basin modeling, it is common to use a zero-depth gravity reference located at the

edges of the basin where bedrock is exposed to determine regional field shape. In this study, field measurements were made using Scintrex CG-5 gravimeters (precision of $1 \mu\text{Gal}$, accuracy of $5 \mu\text{Gal}$) following the methods of *Gettings et al.* [2008]; we used a 6-minute time series and reoccupations of local bases only. Elevation control was achieved through postprocessing of data collected by Trimble GeoXH GPS instrumentation. We observed better than 30 cm vertical accuracy when logging for a minimum of 10 minutes. This procedure resulted in a gravity accuracy of better than 0.1 mGal based on the typical vertical gravity gradient. The IZTC values were computed using routines outlined by *Gettings* [2013] with geometry based on station descriptions and terrain sketches from field notes. The OZTC values were calculated using a global grid routine [*Gettings*, 2013]. Our field data were combined with the Pan American Center for Earth and Environmental Studies (PACES) gravity data, a national gravity and magnetics data repository, for our field areas to provide better data coverage. Reoccupations of historic stations assisted in merging the old and new data sets as well as helped facilitate data quality checks. For consistency, the observed gravity values for historic stations were used and CBGA values were computed directly even though anomaly values are provided by the repository.

In areas of poor data coverage, the gravity field was interpolated using an equivalent-source gridding routine [*Cordell*, 1992]. The gridding routine is designed to interpolate scattered, 3-dimensional, potential-field data in an iterative scheme. Gravity profile transects were then extracted from this new grid, adjusted for regional effects using low-order polynomials with zero-depth reference points, and subsequently modeled using the Semi-Automated Marquardt Inversion code (SAKI) [*Webring*, 1985]. Model control was established using bedrock exposures on the margins of the basins and existing borehole logs in the center (where available).

2.2 Introduction to the Magnetotelluric Method

The magnetotelluric (MT) method [*Tikhonov*, 1950; *Cagniard*, 1953; *Vozoff*, 1991] is a natural source electromagnetic (EM) technique that involves measurement of the two horizontal components of the electric field \mathbf{E} and the three components of the magnetic field \mathbf{H} on the Earth's surface. Natural fluctuations in the magnetic field induce electrical currents at the surface which diffuse downwards into the subsurface. The conductivity structure of the subsurface determines the MT response at a measurement site and modifies the amplitude and phase relationships between the electric and magnetic fields observed at the surface. The MT response is analyzed in frequency and space to make inferences of the subsurface electrical conductivity structure.

The amplitude and phase relationships of the horizontal components of the measured electric and magnetic fields are related as follows:

$$\mathbf{E} = \mathbf{Z}\mathbf{H} \quad (2.12)$$

where the impedance tensor \mathbf{Z} is the electric field complex transfer function and is defined as

$$\mathbf{Z} = \mathbf{X} + i\mathbf{Y} = \begin{bmatrix} Z_{xx} & Z_{xy} \\ Z_{yx} & Z_{yy} \end{bmatrix} \quad (2.13)$$

and the relation can be written in Cartesian coordinates

$$\begin{bmatrix} E_x \\ E_y \end{bmatrix} = \begin{bmatrix} Z_{xx} & Z_{xy} \\ Z_{yx} & Z_{yy} \end{bmatrix} \begin{bmatrix} H_x \\ H_y \end{bmatrix}. \quad (2.14)$$

It is assumed that \mathbf{Z} is a stable property of the subsurface while \mathbf{E} and \mathbf{H} are driven by nonstationary phenomena outside the Earth [*Booker*, 2012]. The vertical component of the magnetic field is related to the horizontal components by

$$H_z = \begin{bmatrix} K_x & K_y \end{bmatrix} \begin{bmatrix} H_x \\ H_y \end{bmatrix}, \quad (2.15)$$

a complex transfer function known as the induction vector [*Parkinson*, 1962] and also commonly referred to as the tipper vector (a measure of the tipping of the magnetic field out of the horizontal plane). In situations where conductivity distribution varies laterally, the real part of the induction vector will point towards the area of highest conductance when following the *Parkinson* [1962] convention.

The impedance data are commonly displayed as values of apparent resistivity ρ_a in Ωm and phase ϕ in plots that are referred to as MT soundings. Apparent resistivity, given by

$$\rho_a = \frac{1}{\mu_o \omega} |Z|^2, \quad (2.16)$$

is the equivalent average resistivity of the uniform half-space where $\mu_o = 4\pi \times 10^{-7}$ and $\omega = 2\pi f$. The impedance phase is given by

$$\phi = \arg(Z) \quad (2.17)$$

which is the angle between the impedance vector and the positive real axis on the complex plane.

Following *Caldwell et al.* [2004], the phase relationships in \mathbf{Z} can be expressed by a second-rank tensor known as the MT phase tensor

$$\mathbf{\Phi} = \mathbf{X}^{-1} \mathbf{Y} = \begin{bmatrix} \Phi_{xx} & \Phi_{xy} \\ \Phi_{yx} & \Phi_{yy} \end{bmatrix}. \quad (2.18)$$

Some advantages of the phase tensor are that it is independent of distortion, no assumptions about the nature or dimensionality of the regional conductivity structure are needed, and details about the preferred orientation of regional structure are easily deduced [*Caldwell et al.*, 2004]. Distortion of the electric field is caused by near-surface heterogeneities and topography [*Jiracek*, 1990]. The phase tensor is independent of the near-surface distortion when the skin depth, δ_m , is larger than the scale of the offending body. The skin depth, δ_m , given in units of meters is defined as

$$\delta_m = 500 \sqrt{\rho_a T}, \quad (2.19)$$

where ρ_a is apparent resistivity in Ωm and T is the period in seconds.

The phase tensor is often represented graphically as an ellipse (Figure 2.1) where the major and minor axes depict the principle axes of the phase tensor and the area inside the ellipse can be colored according to one of the coordinate invariant parameters.

The invariants are as follows

$$\text{tr}(\Phi) = \Phi_{xx} + \Phi_{yy} \quad (2.20)$$

$$\text{sk}(\Phi) = \Phi_{xy} - \Phi_{yx} \quad (2.21)$$

$$\det(\Phi) = \Phi_{xx}\Phi_{yy} - \Phi_{xy}\Phi_{yx} \quad (2.22)$$

These invariants are then re-expressed in the following quantities since any function of an invariant is also coordinate invariant:

$$\Phi_1 = \frac{\text{tr}(\Phi)}{2} \quad (2.23)$$

$$\Phi_2 = [\det(\Phi)]^{1/2} \quad (2.24)$$

$$\Phi_3 = \frac{\text{sk}(\Phi)}{2} \quad (2.25)$$

The minimum and maximum phases (the amplitudes of the principal) are representative of the resistivity gradient in a sampled volume, below and around the station, and are defined by

$$\Phi_{min} = (\Phi_1^2 + \Phi_3^2)^{1/2} - (\Phi_1^2 + \Phi_3^2 - \Phi_2^2)^{1/2} \quad (2.26)$$

and

$$\Phi_{max} = (\Phi_1^2 + \Phi_3^2)^{1/2} + (\Phi_1^2 + \Phi_3^2 - \Phi_2^2)^{1/2}, \quad (2.27)$$

where low values (<1 or $< 45^\circ$ if we take the \tan^{-1}) indicate an increase in resistivity with period and high values (> 1 or $> 45^\circ$ if we take the \tan^{-1}) indicate a decrease in resistivity with period. In the case of 1D structure ($\Phi_{max} = \Phi_{min}$), the phase tensor is a circle and in a uniform half-space ($\Phi_{max} = \Phi_{min}=1$), it is a unit circle [Heise *et al.*, 2006].

Dimensionality of the data can be inferred by the amplitude of the skew angle

$$\beta = \frac{1}{2} \tan^{-1} \left(\frac{\Phi_{xy} - \Phi_{yx}}{\Phi_{xx} + \Phi_{yy}} \right) \quad (2.28)$$

which is a measure of the tensor's symmetry. *Caldwell et al.* [2004] asserts that in the general case, $\beta = 0$ is a necessary but not sufficient condition for 2D regional conductivity structure. What should be sought is a range of frequencies where β is

zero within the observational errors and the direction of the phase tensor major axis is constant [Caldwell *et al.*, 2004]. Booker [2012] suggests that for 2D interpretation of quasi-2D structure, it is reasonable to have a normalized skew $|\psi| \leq 0.1$ radians or less than 6° , where $\psi = 2\beta$. This implies that $|\beta| \leq 3^\circ$ is effectively the condition $\beta = 0$ within its uncertainties. Another parameter of the phase tensor is the reference axis (coordinate dependent) which is defined as

$$\alpha = \frac{1}{2} \tan^{-1} \left(\frac{\Phi_{xy} + \Phi_{yx}}{\Phi_{xx} - \Phi_{yy}} \right) \quad (2.29)$$

where $\alpha - \beta$ gives the direction of the major axis of the phase tensor ellipse and is aligned either parallel or perpendicular to the strike of the conductivity distribution.

In a setting that is 2D, the electric field is linearly polarized parallel or perpendicular to the strike of the regional conductivity distribution and separates into two independent modes [Wannamaker *et al.*, 2008]. These polarizations of parallel and perpendicular to strike are known as the transverse electric (TE) and transverse magnetic (TM) impedances, respectively. If we define geoelectric strike as the x direction, then in the TE mode, $E_x = Z_{xy}H_y$, $H_z = K_yH_y$ and electric current flows parallel to strike and in the TM mode, $E_y = Z_{yx}H_x$ and current flows perpendicular to strike. However, if we have no knowledge as to which of the maximum or minimum phases of the MT phase tensor corresponds to the TE or TM polarization, the 90° ambiguity remains [Caldwell *et al.*, 2004]. The induction vector, discussed above, is useful in resolving the ambiguity of the phase tensor in regards to the regional strike direction.

Coherency and quality of the data can be visually checked by plotting the phase tensor ellipses of each transect side-by-side or in a map view for each period. There should be clear trends, patterns or groupings of similarity both spatially and by period. Any variation in the phase tensor parameters should be smooth and continuous for periods sensing a common volume. Abrupt changes are most likely an indication of a poor/noisy data quality.

The MT modeling was done with a 2D inversion code [Wannamaker *et al.*, 1987; Tarantola, 1987; de Lugao and Wannamaker, 1996] using the TM mode with the induction vector. The TM mode with the induction vector is selected since they

are both less susceptible to finite strike length effects than the TE mode. Viability of TM models arises from the inclusion of boundary charge effects from current flow along resistivity gradients [Wannamaker *et al.*, 2008] and the TM mode explicitly includes discontinuities in its formulation [Wannamaker, 1999]. Geoelectric strike direction was determined using phase tensor geometry, induction vectors, and complete Bouguer gravity anomalies. At only a few of the MT stations, electric field distortion was significant and so it was removed following the methods of Bibby *et al.* [2005]. Afterwards, the data were rotated to strike and subsequently modeled in the inversion program. The 2D domain is 129 x 49 nodes with a minimum discretization of 200 m in a multiresolution grid. Initial starting models consisted of a homogeneous half-space of 400 Ωm . Multiple inversions were done using different starting models to verify the stability of the final solution model with a target nRMSE of < 2.0 .

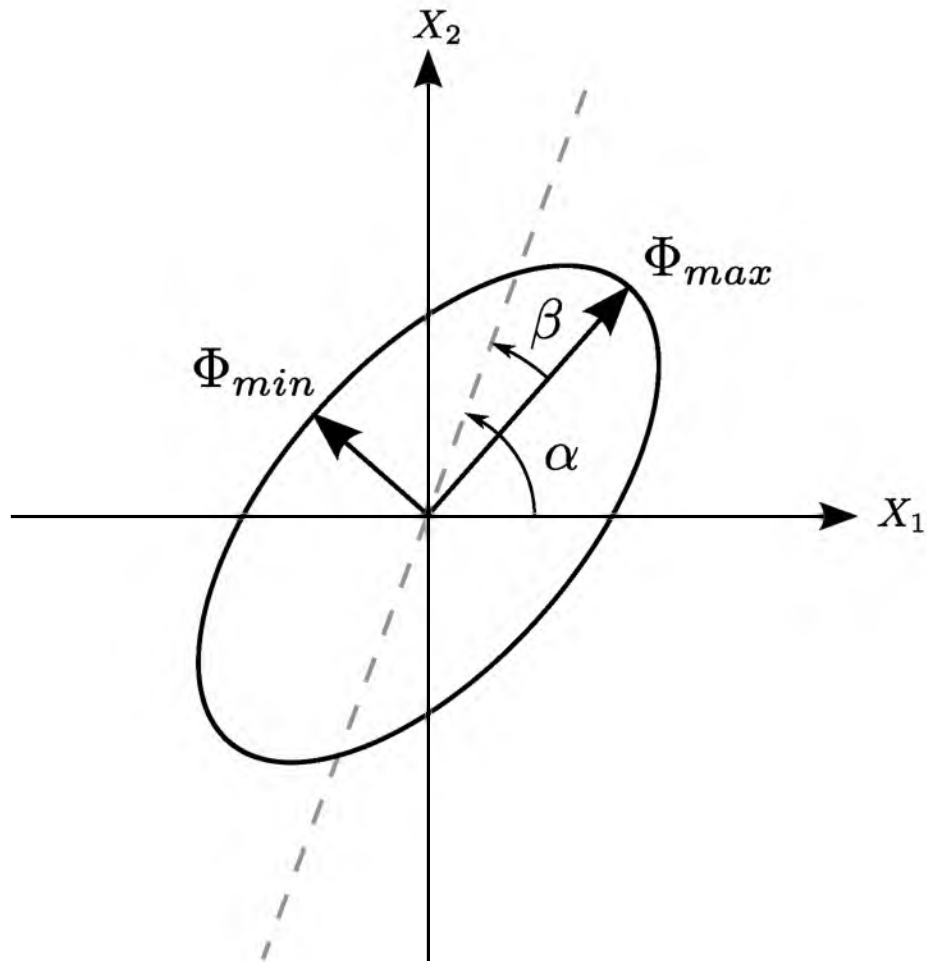


Figure 2.1. Graphical representation of the phase tensor as an ellipse. Ellipse properties are determined by three coordinate invariant parameters and one dependent parameter. Modified from *Caldwell et al.* [2004].

CHAPTER 3

CRATER BENCH

3.1 Introduction

Abraham Hot Springs (a.k.a. Baker or Crater Hot Springs) is located at the eastern margin of the Pleistocene age (0.9 Ma) Crater Bench basalt flows 28 km northwest of Delta, Utah (Figure 3.1). The basalt flows overlay lacustrine and fluvial sediments of the Sevier Desert. Temperatures in the flowing springs reach as high as 87°C and flow rates have been estimated at between 5400 and 8400 lpm [Rush, 1983]. In regard to the summit of Fumarole Butte, the remnant volcanic vent, *Gilbert* [1890] noted that "about the outer edge of the summit there are 30 or 40 crevices from which warm, moist air gently flows," which "testifies to a residuum of volcanic heat in the old flue." Fluid analysis by *Rush* [1983] suggests that the hot spring water may be 50 % mixed with nonthermal water and the hot water component could be 140°C. The geological structure controlling the hydrothermal system is unknown and the reservoir temperature is uncertain according to *Blackett* [2007]. It has been hypothesized by *Mundorff* [1970] that water may have been heated by a high geothermal gradient or by contact with a cooling volcanic body and that conduits in the volcanic flow or concealed faults in the vicinity of the springs may furnish the avenues for deep circulation and emergence of water. Early petrologic studies done by *Peterson* [1979] describe the volcanic complex as being comprised of basaltic andesite flows, a tholeiitic basalt body, and a rhyolite flow with two obsidian exposures. Using K-Ar age-dating techniques, *Peterson* [1979] dated the basaltic andesite, tholeiite, and rhyolite at 0.88, 6.0 and 6.1 Ma, respectively. We attempt to resolve some of these uncertainties in this study, primarily those attributed to structure.

3.2 Gravity

3.2.1 Survey and Modeling

Gravity measurements in the vicinity of Crater Bench were previously reported in the work of *Smith* [1974]. A total of 88 new gravity stations were established during a 2 week period in the summer of 2010 (Figure 3.2) in order to achieve better coverage adjacent to MT stations. Stations established on top of Crater Bench were spaced from 1 to 1.5 km and traverses of the mud flats area adjacent to the lava flows have an in-line station spacing of 1.25 km with 3 km interline offsets.

A simple 2D gravity model of transect AB (Figure 3.3) was created using three lithologies to represent the basalt flows, sediment fill, and basement rock. Their respective densities of 3.0, 2.2, and 2.7 g cm⁻³ were based on average values for the appropriate lithology from regional geology reports and logs of nearby deep wells [*Hintze and Davis*, 2003; *Peterson*, 1979]. Although the actual thickness of the Crater Bench basalt flows is unknown, the modeled thickness is constrained between 60 and 100 m, consistent with the observed topographic relief at the surface.

3.2.2 Results

The complete Bouguer gravity anomaly, in Figure 3.2, shows a local gravity high of -165 mGal centered below Abraham Hot Springs (AHS) spanning 20 km north-south and 10 km east-west. A relative gravity low of 15 mgal is present just east of the gravity high, but a more significant low of 20 mgal is located to the northwest.

The 2D gravity model of transect AB (Figure 3.3) displays a deep sedimentary fill of 3.4 km at the western end of the profile which gently climbs in the eastward direction until reaching a minimum sediment depth of 1.5 km roughly coincident with the location of AHS and the edge of the Crater Bench basalt flows. Basement then dips eastward steeply into a small trough. On the residual gravity values, a small amplitude, high-frequency signal is observed on the dominant lower-frequency signal located at both 343 and 350 km eastings. These high-frequency signals are due to near-surface structure and are caused by the large, lateral density contrast between the basalt flows and the sedimentary fill.

3.3 Magnetotellurics

3.3.1 Survey and Modeling

A total of 50 MT soundings spread over an area of approximately 200 km² (Figure 3.4) were completed during the summer of 2010. Average station spacing was 2 to 3 km, with occupation times of 12 to 24 hours. Measurements were made both on the basalt flows as well as the surrounding desert area. Graphical representation of the MT phase tensor is shown in Figure 3.5 for periods of 0.027, 0.320, 3.250, and 10.240 seconds using the invariant Φ_2 as the fill color. The shorter period data display mostly 1D characteristics with the majority of tensors being indistinguishable from circles (i.e., only slight differences in lengths of the principal axes). Ellipticity of the tensors increase at longer periods, indicating the data are no longer 1D and are transitioning into 2D/3D domains. In Figure 3.5a, high values of Φ_2 are mostly localized on top of Crater Bench whereas stations that are distal show more moderate Φ_2 values. This behavior is most likely due to the resistivity contrast between the resistive basalts and the conductive underlying sediments. At the period of 3.413 seconds (Figure 3.5c), nearly all of the phase tensors are ellipses with a strong northwest orientation and low Φ_2 values. The volume being sampled at this period is most likely the resistive basement structure. Based on the preferred orientation of the phase tensors and the gravity anomaly field, a preliminary strike trending northwest was inferred.

For select stations chosen for the transect lines shown in Figure 3.4, the strike was calculated from the phase tensors and is shown in Figure 3.6. Since 1D data do not have a strike direction, the very short period data were removed from the computation. All three lines show a preferred strike of approximately 20° or 110° (considering the 90° ambiguity). The information about the coherency and quality of the data used in each transect is gathered by visual inspection from stations that are located near each other, shown in Figure 3.7. From the Φ_2 values, we can see that a more conductive layer is detected in the shorter periods for portions of line 2 and line 3. In Figure 3.5, these stations are located near the center of Crater Bench.

Moderate values of Φ_2 at 5.120 seconds indicates little or no gradient in resistivity structure and most likely is sampling well into the resistive basement rock.

Dimensionality of each of the Crater Bench MT transect lines based on skew angle β is shown in Figure 3.8. There is a negligible skew value for shorter periods but skew starts becoming significant for both lines 2 and 3 just before reaching a 10-second period. Widespread large skew values are a reasonable indicator for 3D conditions. However, there are some outliers which point to noisy data measurements which is not entirely unexpected. All three lines contain a few noisy data points. Since we observe 2D behavior in the data up to periods of 10 seconds followed by 3D behavior, we exclude data at periods longer than 10 seconds as well as any noisy data points.

3.3.2 Results

The MT inversion lines (Figure 3.9) display a high resistivity structure ($> 100 \Omega\text{m}$) rising gently from the west and dipping steeply to the east. Intermediate resistivity bodies of 10 to $100 \Omega\text{m}$ lay immediately above this deep structure and are covered by localized low-resistivity bodies of 5 to $10 \Omega\text{m}$ in certain areas. Lenticular bodies of 300 and 500 m thicknesses and very low resistivity are observed at the western ends of lines 2 and 3 covered by a thin, high-resistivity body near the surface (Figures 3.9b and 3.9c). The nRMSE values of the 2D inversion models are between 0.7 and 1.0 which is quite good for field data.

3.3.3 Thickness of Basalt Flows

As a simple exercise, we can attempt to constrain the thickness of the basalt flows by using geophysical as well as topographical observations. Previous estimates of the thickness of the Crater Bench basalt flows range from 45 to 90 m [Johnson, 1975] and 90 to 150 m [Smith, 1974], varying by location investigated. In this work, the basalt flows have been modeled at a thickness between 60 and 90 m which fits well in the 2D gravity model. In a 1D forward computation using the Bouguer slab approach eq(2.8), the gravity signal resulting from 60 to 100 m thicknesses is approximately 2 to 3 mGal which is quite small compared to the more dominant local signals (Figure 3.2).

Furthermore, 1D inversions of the MT data were completed for stations located on the basalt flows and compared to the elevations shown in Figure 3.10. It appears that the basalt thicknesses obtained from 1D inversion models of the MT data fit the topographic observations for these same locations. This indicates that the topographic relief of the basalt flows is a fair representation of the overall thickness. From the elevation and 1D MT models, the majority of the basalt flows range in thickness from 50 to 100 m.

3.4 Discussion

The dominant structure in the 2D gravity model (Figure 3.3) is the basement configuration. The shape of the modeled basement high bears great resemblance to an uplifted horst block. Depth-to-basement estimates based on this model range from 1.5 to 3.4 km and are quite similar to 2D MT model estimates of 1.3 to 3.6 km. Due to the nonuniqueness inherent in gravity modeling and the lack of control points in the immediate area of Crater Bench, the depth-to-basement may be less than what is indicated in the 2D gravity model. Fine tuning of model densities will improve the approximation, although deep geometry should not change drastically in this case since MT models are in good agreement.

The high-resistivity structure at depth in the MT models is interpreted as basement rock (marbleized Cambrian limestone and dolomite) yielding depth-to-basement estimates ranging from 1.3 to 3.6 km. Intermediate-resistivity bodies are interpreted as sedimentary rocks and fill and low-resistivity bodies are interpreted as clay-rich sediments. The thin, high-resistivity body at the surface is interpreted as the basalt flows which correlates well spatially with the surface geology and is within unweathered-basalt resistivity values ($> 1000 \Omega\text{m}$) suggested by *Palacky* [1988]. The underlying conductors may be clays generated by hydrothermal alteration, hot saline fluids, or a combination thereof.

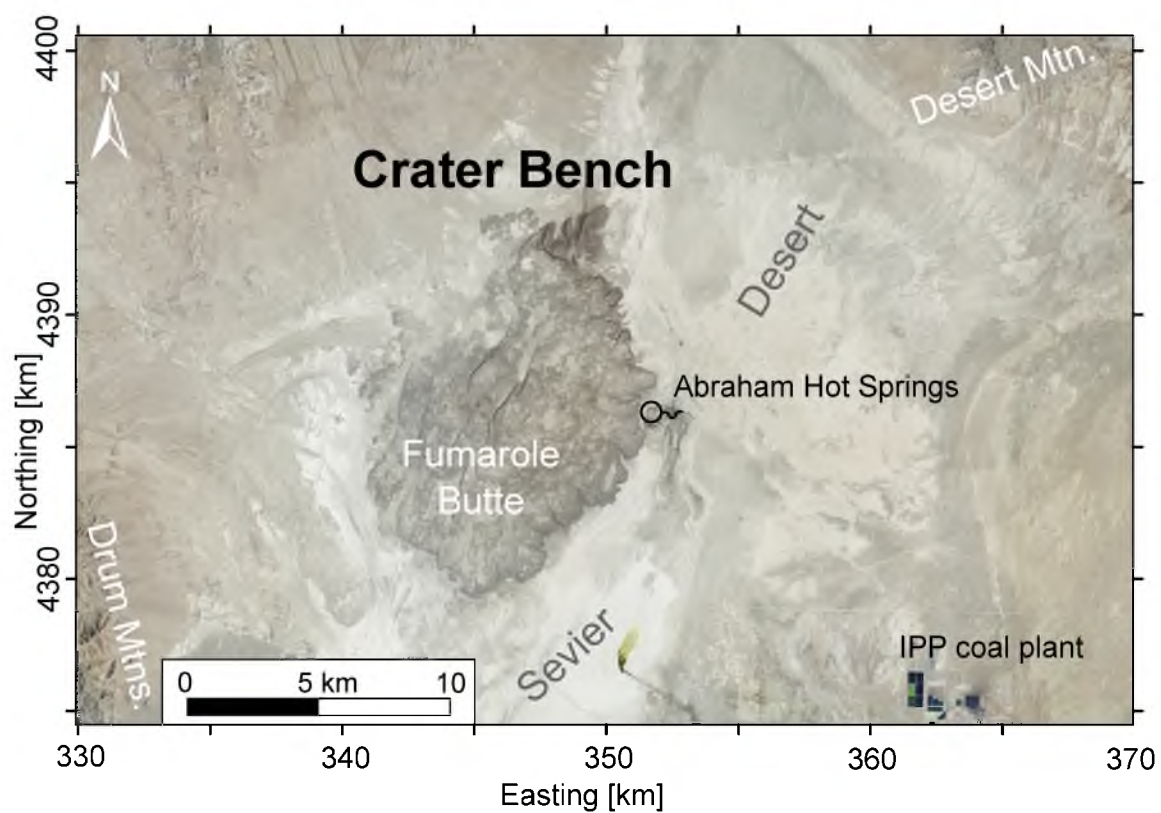


Figure 3.1. Map of Crater Bench study area. Abraham Hot Springs location indicated by black spring symbol.

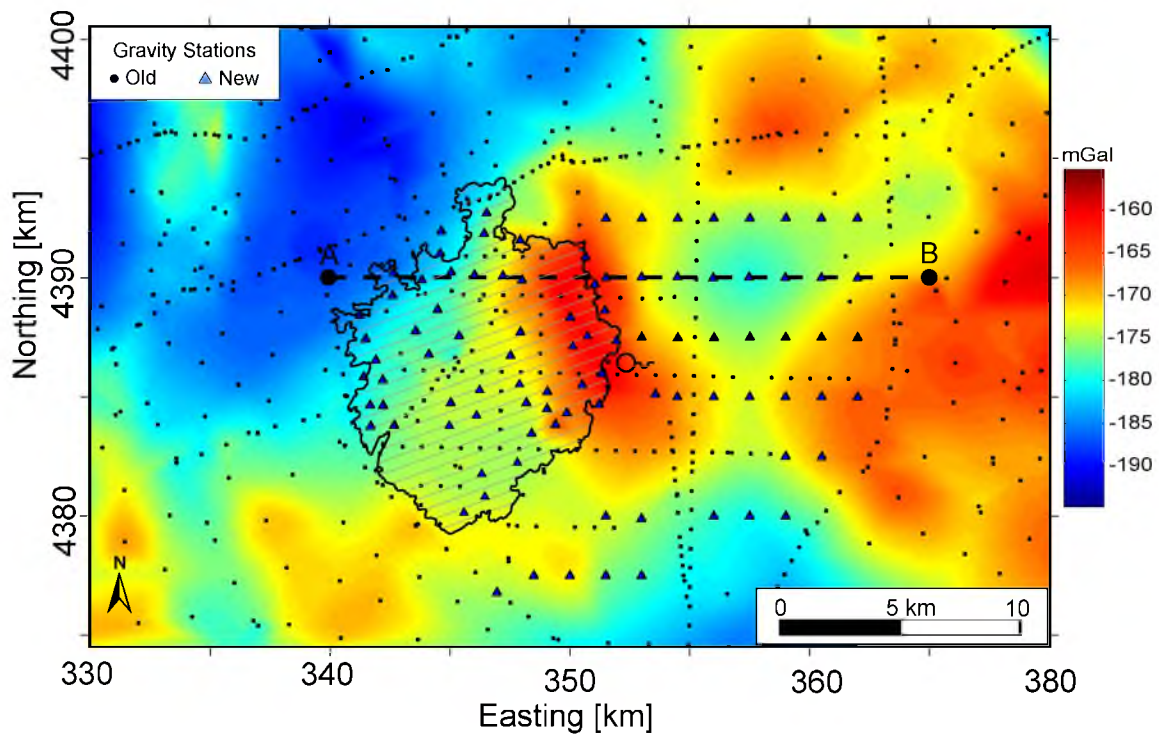


Figure 3.2. Complete Bouguer gravity anomaly map of the Crater Bench study area. Black dashed line AB is gravity model transect, black hatched area outlines the surface extent of the Crater Bench basalt flows and the Abraham Hot Springs location indicated by black spring symbol.

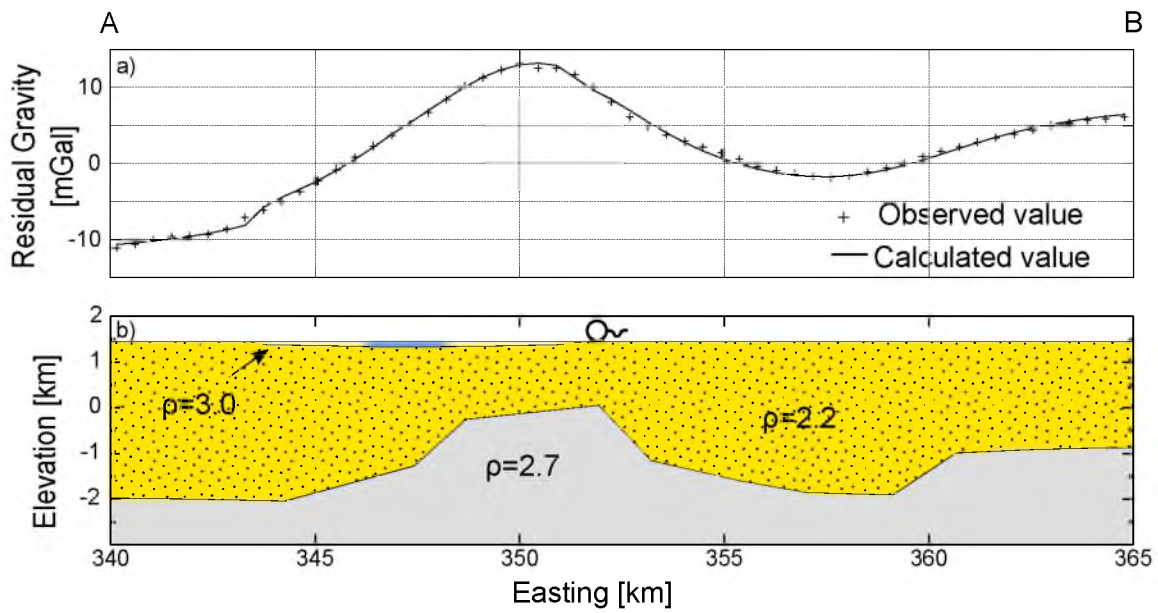


Figure 3.3. Crater Bench gravity transect AB. Residual gravity (a) and 2D gravity model (b) for transect AB. The blue, yellow, and gray colored lithologies are the crater Basalt flows, sedimentary fill, and basement rock, respectively. Densities are given in units of g cm⁻³. Location of Abraham Hot Springs indicated by black spring symbol.

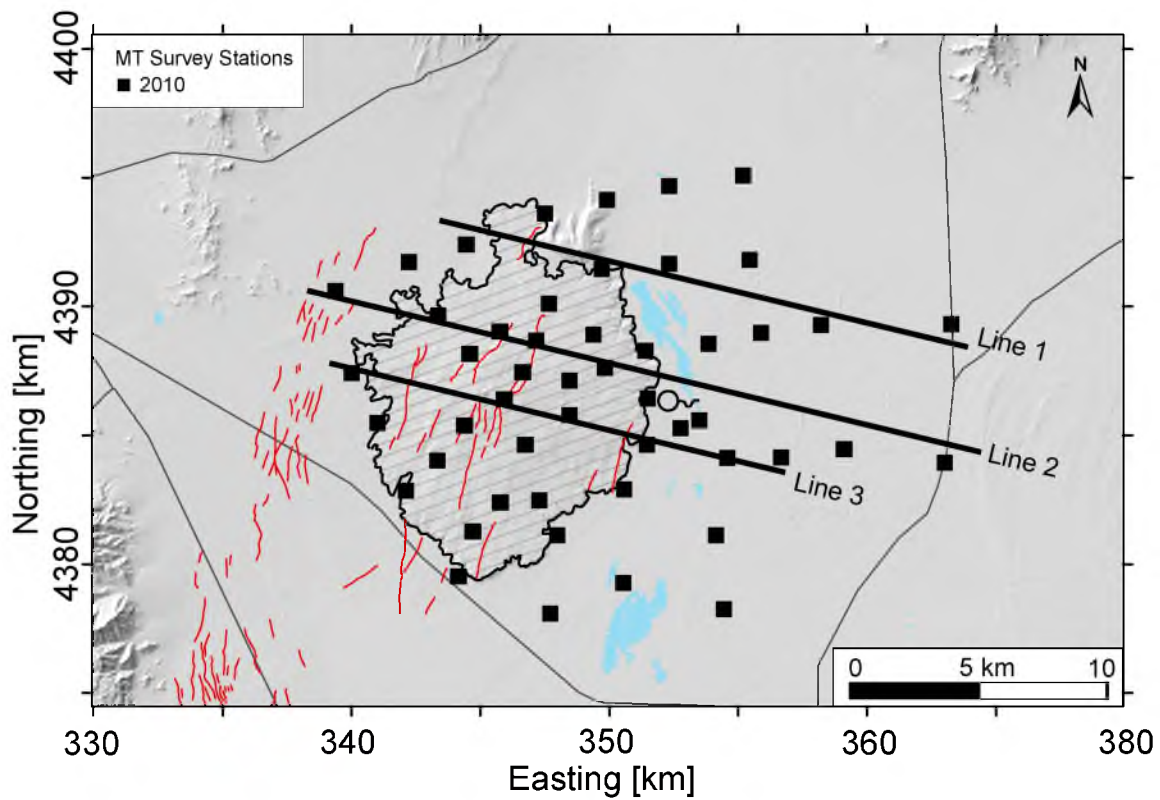


Figure 3.4. Crater Bench MT survey area. Solid black squares show MT stations, black hatched area outlines surface extent of the Crater Bench basalt flows, red lines denote Quaternary faults, bold black lines are MT 2D model transects, and gray lines are local roadways. Location of Abraham Hot Springs indicated by black spring symbol.

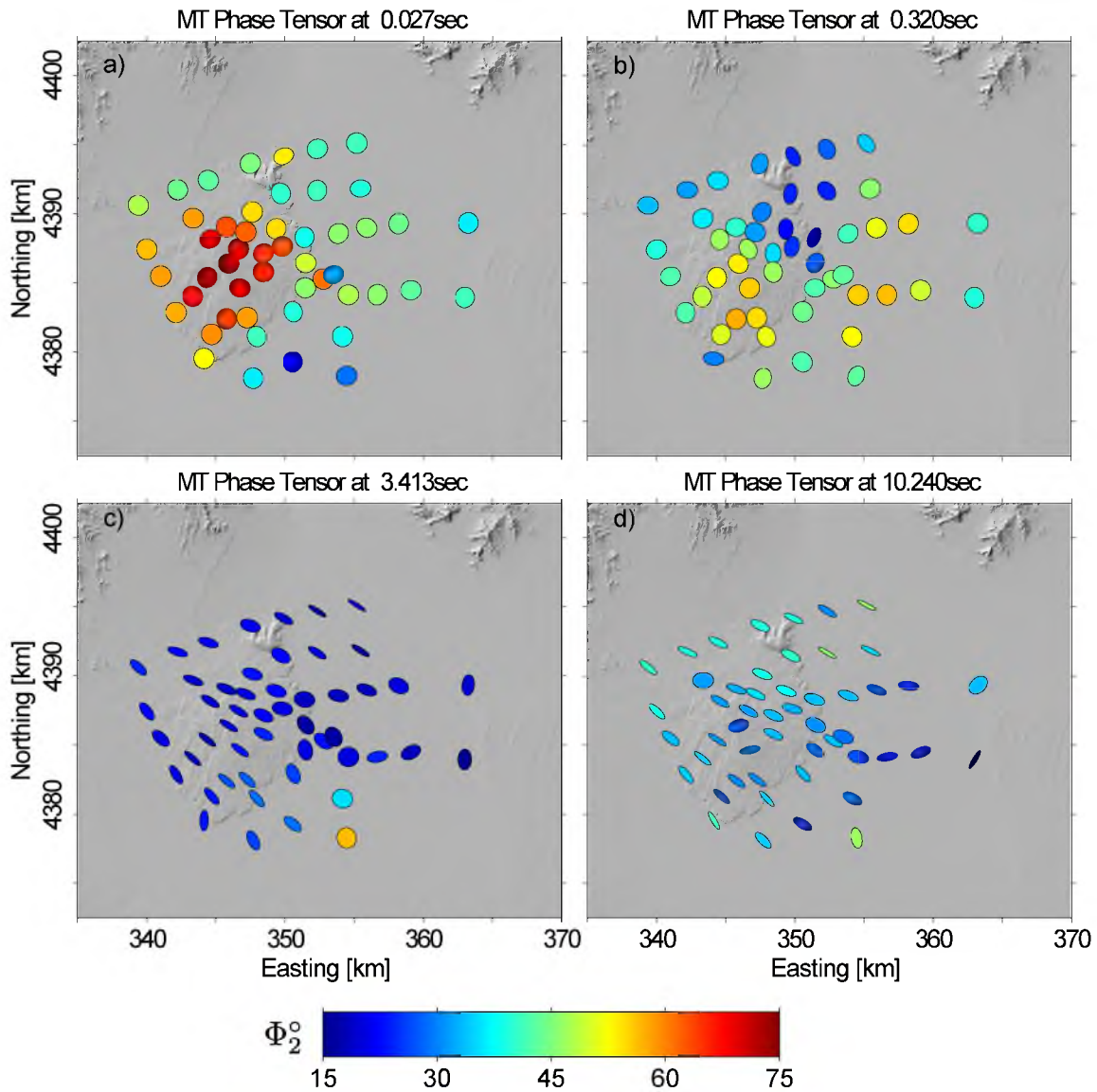


Figure 3.5. MT phase tensor ellipse maps for select periods (a,b,c,d) of the Crater Bench MT survey. Phase tensors at shorter periods are circular, indicating 1D conditions and change to ellipses at longer periods, indicating 2D and 3D conditions. Phase tensor color is the geometric mean of the minimum and maximum phases and indicates the conductivity gradient of subsurface structure (i.e., $< 45^\circ$ more resistive and $> 45^\circ$ more conductive).

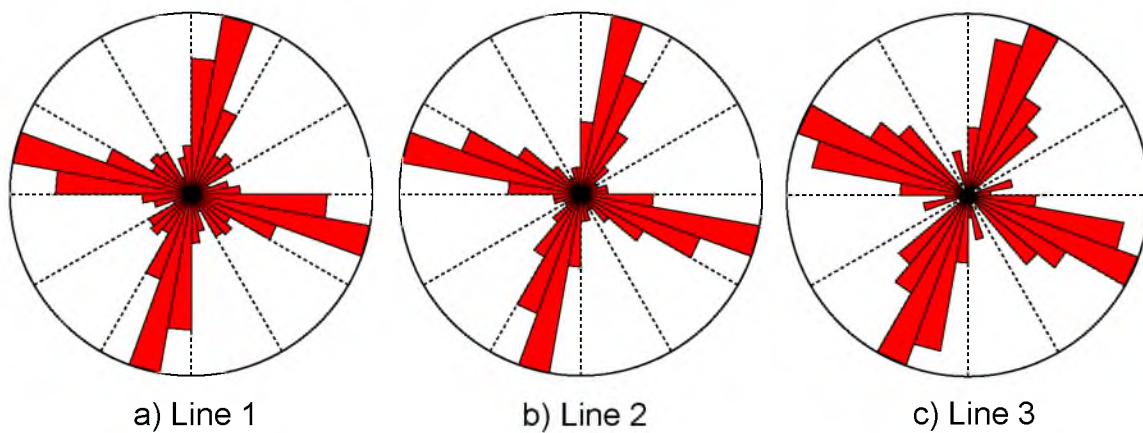


Figure 3.6. Strike directions of Crater Bench MT transect lines. Directions for each transect line (a,b,c) are in geographic coordinates and computed from phase tensor parameters. A consistent trend of azimuth 20° (or 110°) is observed for all lines.

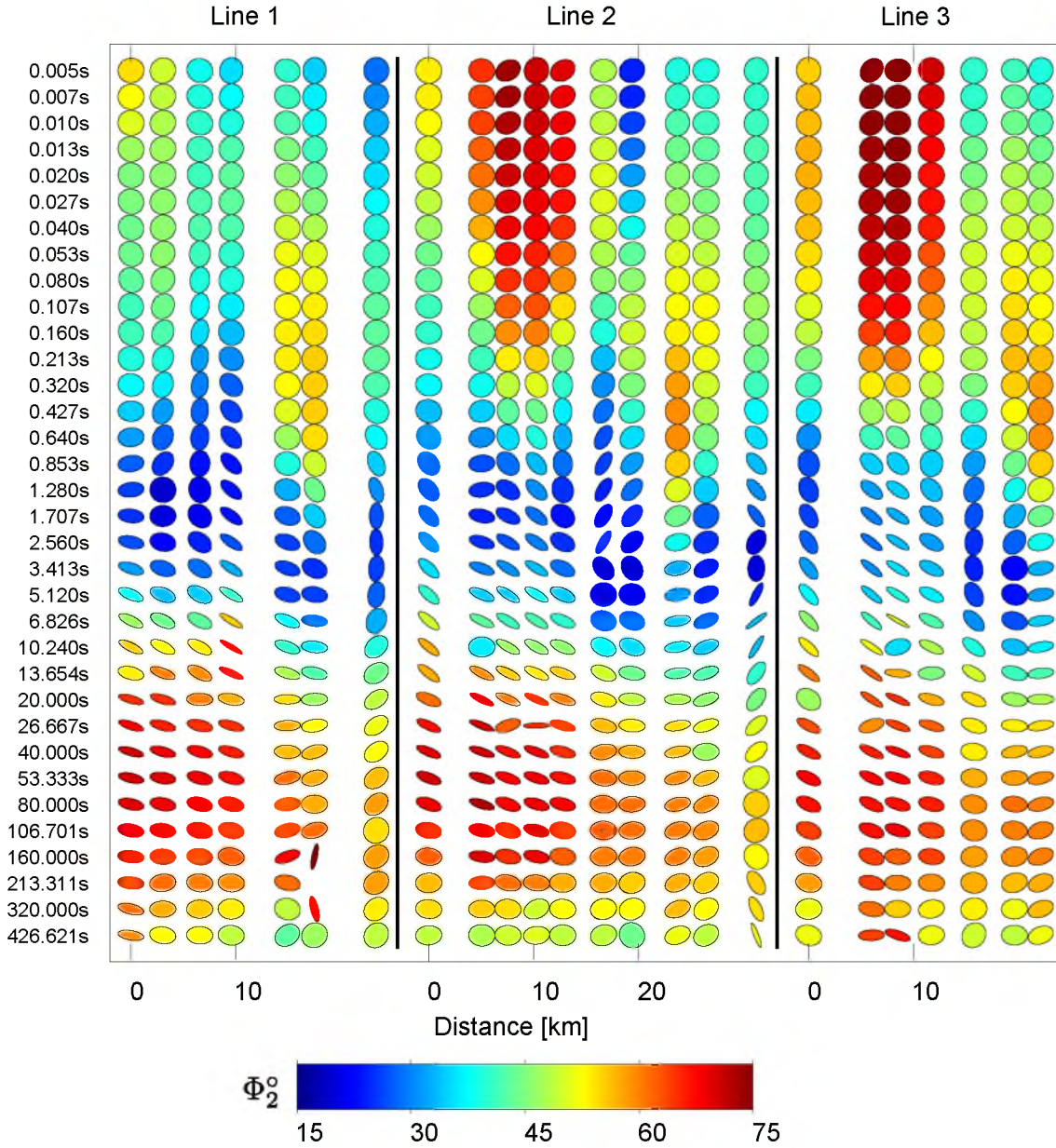


Figure 3.7. Phase tensor ellipses for Crater Bench MT transects. Ellipses are arranged by transect line and period. Phase tensors at shorter periods are circular, indicating 1D conditions and change to ellipses at longer periods, indicating 2D and 3D conditions. Phase tensor color is the geometric mean of the minimum and maximum phases and indicates the conductivity gradient of subsurface structure (i.e., $< 45^\circ$ more resistive and $> 45^\circ$ more conductive). High phase values at short periods in lines 2 and 3 indicate a near-surface conductive structure underneath the basalts near the central area of Crater Bench. Resistive basement is reached in the data at periods around 1 second.

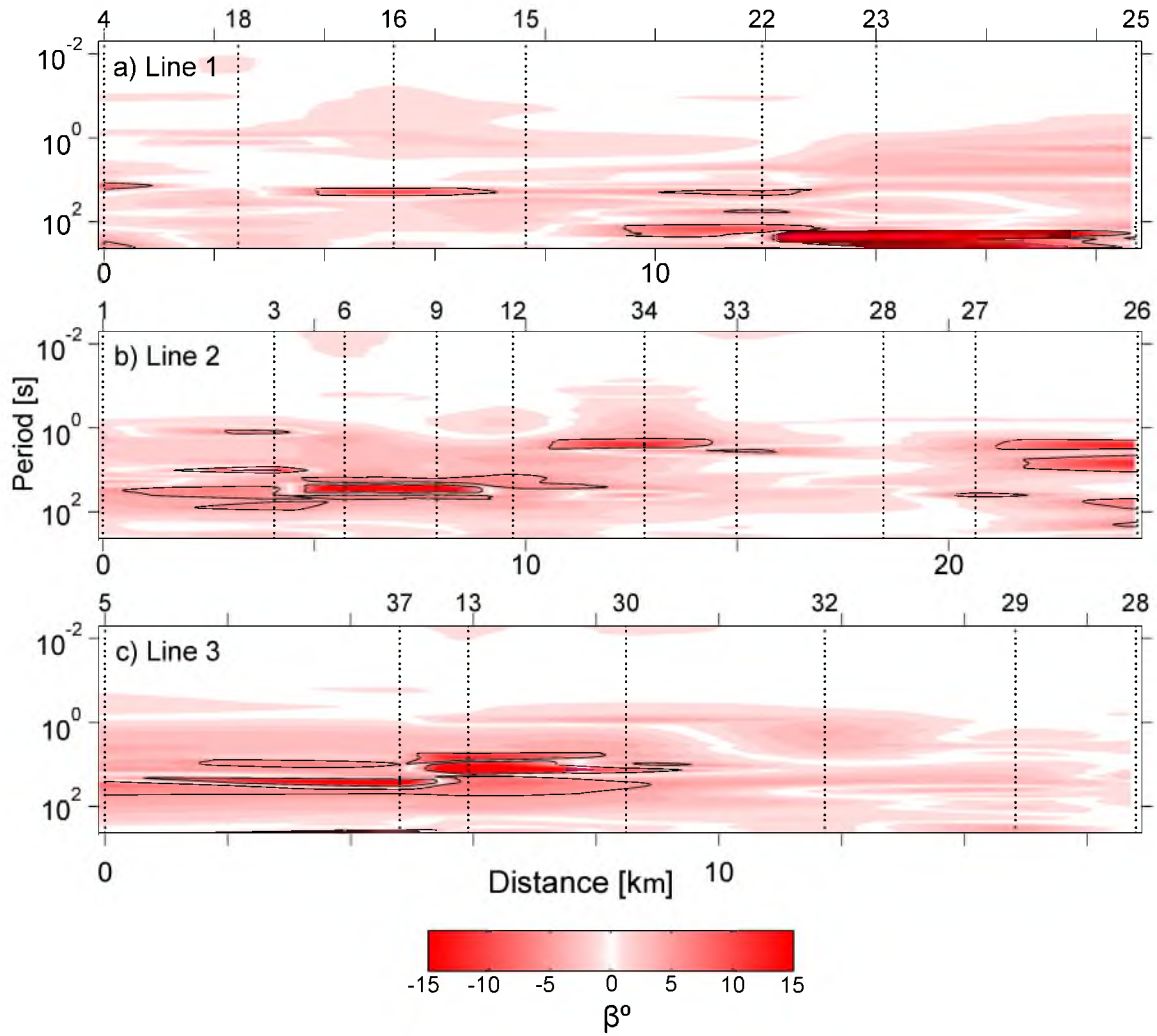


Figure 3.8. Dimensionality for MT transects (a,b,c) of Crater Bench. Skew angle is a phase tensor parameter that assists in distinguishing 2D and 3D data. Contours shown are for -5/+5 skew values; outside of this range, the data are most likely 3D. Aside from some outliers, the data are considered 2D up to a 10 second period where skew indicates they are 3D.

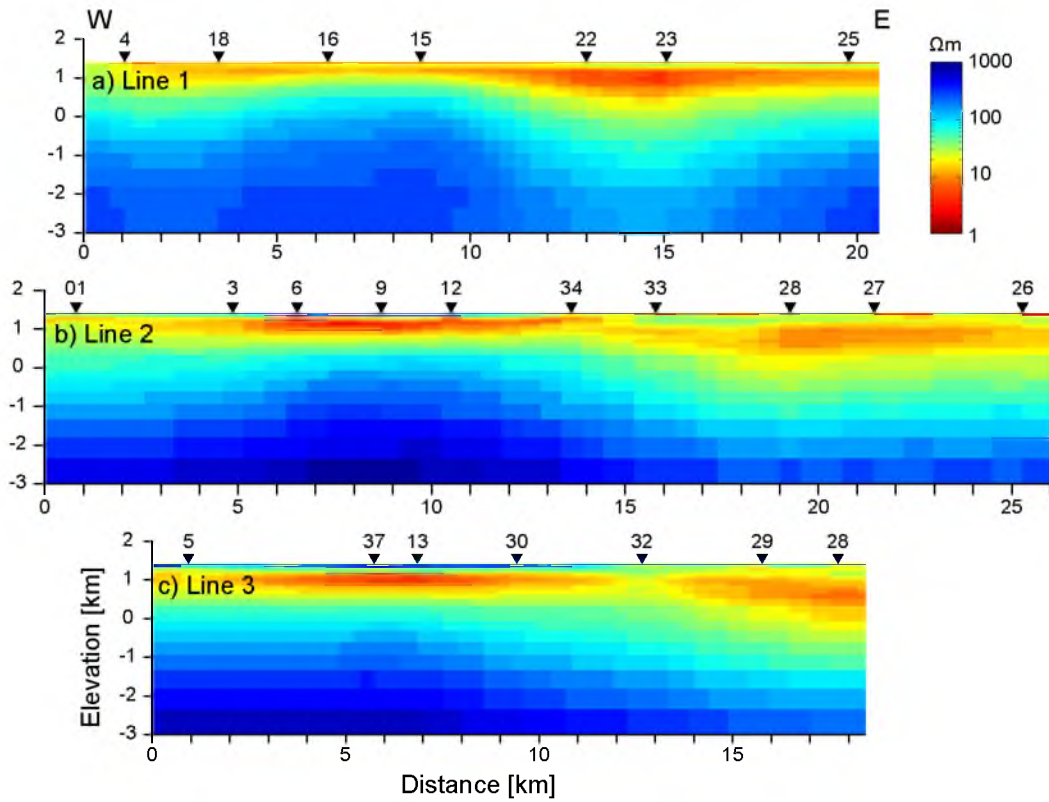


Figure 3.9. Two-dimensional MT resistivity models for Crater Bench. Profile locations (a,b,c,d) are shown in Figure 3.4. MT stations are indicated by black, inverted triangles with station numbers shown. Models were created using the 2D inversion program of *Wannamaker et al.* [1987] with TM mode and induction vector data. Final nRMSE values are 0.7, 1.0, and 1.0 for each line, respectively.

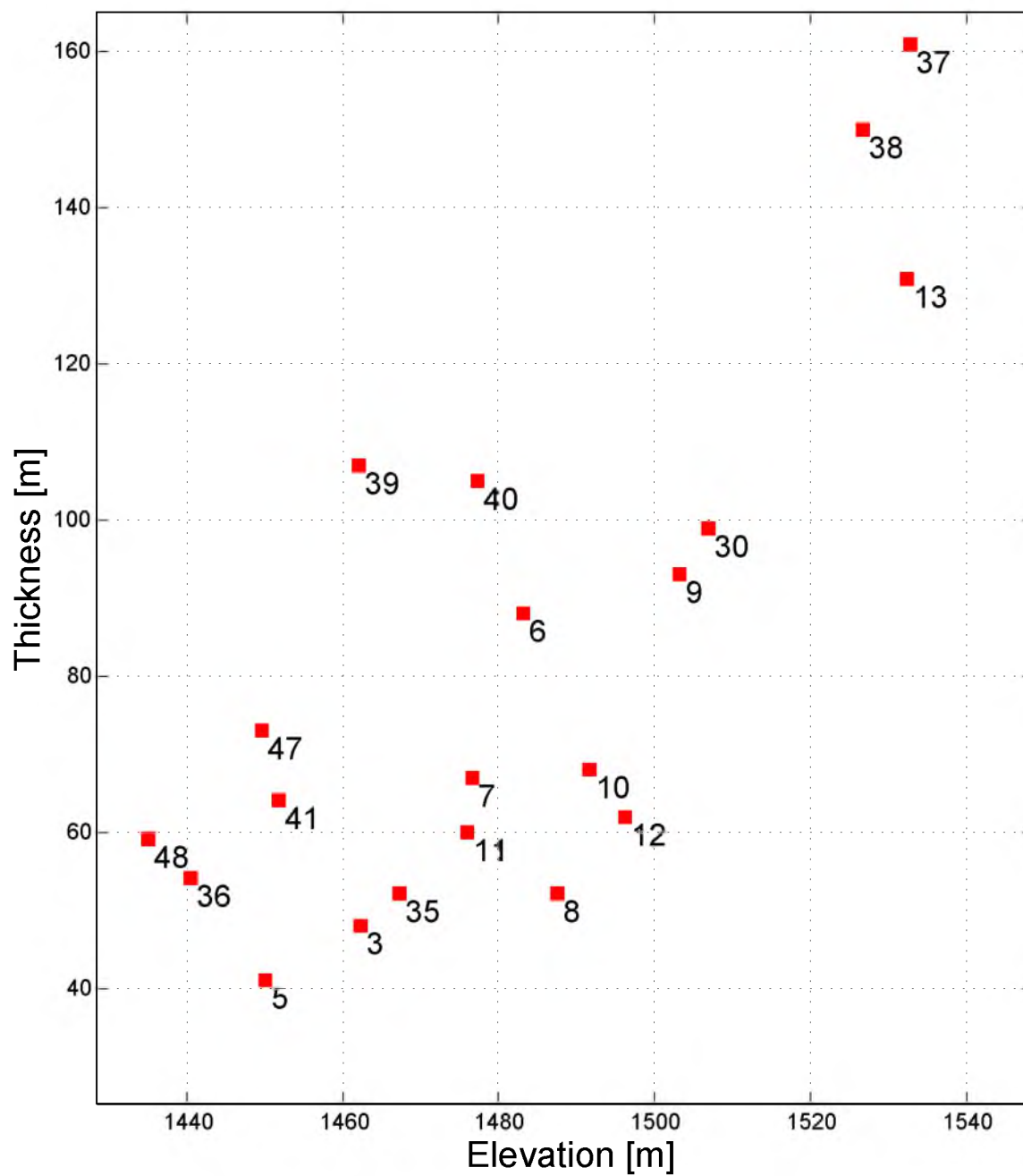


Figure 3.10. Elevation and thickness for Crater Bench basalt flows at select MT stations. Plot of topographic elevation vs. basalt thickness from 1D MT inversion models for MT stations located on top of the basalt flows. Station number indicated.

CHAPTER 4

PAVANT BUTTE

4.1 Introduction

The Black Rock Desert (Figure 4.1) lies within the boundaries of the Sevier thermal area, which contains most of Utah's high and moderate temperature geothermal systems [Blackett, 2007]. The Black Rock Desert has experienced extensive volcanism ranging in age from greater than 9 Ma to as recent as 600 years ago [Hintz, 2008]. Heat-flow values in the Pavant Butte area are 100-105 mW m⁻², 10-15 mW m⁻² higher than the typical 90 mW m⁻² of the northern Basin and Range. Allis *et al.* [2011] suggest that stratigraphically-hosted geothermal reservoirs likely exist in the deep basins of the Basin and Range having heat-flow values of 80-100 mW m⁻² with thick blankets of low thermal conductivity Oligocene to Pleistocene sediments. Similar areas of higher than normal heat flow, such as Pavant Butte, would result in still higher temperatures of the stratigraphic reservoirs at depth resulting in more attractive exploration targets.

Corrected temperatures encountered at the bottom of the Pavant Butte 81-7 well (Figure 4.2) were in excess of 220°C. Temperatures logged in other deep wells in the Black Rock Desert appear to be significantly cooler (about 100°C less) at similar depths. For the southern wells in the area, their low temperatures can be explained by the documented loss of massive amounts of drilling fluid and mud to fracture zones during drilling. These losses likely led to greater than normal cooling of the well bore and surrounding rock and consequently, measured temperatures are probably under-corrected. For the remaining wells in the Black Rock Desert, the lower temperatures at depth are due primarily to thermal conductivity effects (see Allis *et al.* [2011, 2012]).

4.2 Gravity

4.2.1 Survey and Modeling

A total of 168 gravity stations were established during a 3-week period in the summer of 2011 (Figure 4.3) to supplement previous gravity observations. A station spacing of approximately 2 km in a grid-like layout was adopted in order to achieve better coverage in areas adjacent to MT observations. For the gravity profile transect CD, a spacing of 1 km was used where possible to increase data resolution for 2D modeling.

A simple 2D gravity model of transect CD (Figure 4.4) was developed for a variable thickness sedimentary layer overlying basement rock. Their respective densities of 2.2 and 2.7 g cm⁻³ were held constant, based on average values for the appropriate lithology from regional geology reports and logs of nearby deep wells [*Hintze and Davis, 2003*]. The Pavant Butte 81-7 exploration well (Figures 4.3 and 4.4) was used as a control point for sediment thickness as well as a check for model densities. This well penetrates 9770 feet (2,978 m) of Oligocene and Pleistocene sediments before reaching the Cambrian basement [*Hintze and Davis, 2003*].

4.2.2 Results

The complete Bouguer gravity anomaly map (Figure 4.3) shows that the basin-related anomaly is fairly symmetric about a north-south trending axis. The prominent north-trending gravity low of -40 mGal and approximately 20 km wide is bounded by gravity highs to the east and west. The 2D gravity model of transect CD (Figures 4.3 and 4.4) fits a local signal of amplitude > 30 mGal with the lowest values east of profile center. The model shows a nearly symmetric, gently dipping basement interface with maximum depth of 3 km found at approximately 357 km easting. The western and eastern basement interfaces appear to be roughly symmetric.

4.3 Magnetotellurics

4.3.1 Survey and Modeling

A total of 73 MT soundings spread over an area of approximately 2000 km² (Figure 4.5) were completed during the summer of 2010. The average station spacing is 2 to 3 km, station occupation times were 12 to 24 hours. In 2012, an additional 34 MT stations were added to the southwestern area of the Black Rock Desert. The extended data are not presented here but will be merged with the current dataset and analyzed in the future.

Graphical representation of the MT phase tensor for periods of 0.027, 0.320, 3.250, and 10.240 seconds is shown in Figure 4.6. The shorter period data displays mostly 1D characteristics with the majority of tensors being indistinguishable from circles; there are only slight differences in lengths of the principal axes. At longer periods the ellipticity of the tensors increases, most notably near the margins of the basin, indicating the data are no longer 1D and are 2D/3D. The invariant Φ_2 of each tensor is used as the fill color and low values indicate the subsurface is more resistive with longer periods. With the change in the shape of the phase tensors and the low Φ_2 values observed at the margins, it is apparent that the MT data are progressively sampling the resistive basement structure. A preliminary geoelectric strike direction was estimated at an azimuth of 355° by using the gravity anomaly signature of the basin. For select stations chosen for the transect lines (Figure 4.5), the strike was calculated from the phase tensors and shown in Figure 4.7. Since 1D data do not have a strike direction, the very short period data were removed from the computation. All three lines show a preferred strike of approximately 350° or 80° (considering the 90° ambiguity). The coherency and quality of the data used in each transect are visually inferred from Figure 4.8 and appear to be quite good. Most changes are a smooth, gradual variation and occur at places where we have expected them to happen from known geology. From the Φ_2 values, we can see that a more resistive layer is detected first near the ends of each transect which is interpreted as basement rock.

Dimensionality of each of the MT transect lines based on skew angle β is shown in Figure 4.9. In general, a nonzero skew for the shorter periods is typically nonexistent and starts becoming appreciable around the 10-second period, indicating 3D conditions or quite possibly noisy data in the instance of isolated occurrences. In either case, the known local basement depths are still within the range of probable skin depths (δ_m) for this period of MT data, so the application of 2D inversion is not invalidated. The 2D assumption is further supported by the strong 2D geometry of the basin which is observed in both the topographic and gravity data.

4.3.2 Results

The MT inversion models are all roughly symmetric and quite similar in appearance with a low-resistivity body ($< 10 \Omega\text{m}$) centered deeply on each transect (Figure 4.10). The low-resistivity zone broadens and thins, relatively, to a 1 to 2 km thickness with decreasing depth. High-resistivity structures seem to bound this conductive structure at depth near the edges of the models. Very thin, high-resistivity layers are observed at the surface of the models and appear to be more extensive in lines 1 and 2. The low-resistivity structure extends to the bottom of the model space which could be a side effect of the intentional truncation of the data at the 10-second period. Since the skin depth δ_m for apparent resistivities of 1 to $10 \Omega\text{m}$ would be between 1.5 and 5 km, it is possible that the data are being overextended in the model space. This overextension of data could result in a downward smearing effect in the model. The nRMSE values of the final 2D inversion models are between 1.8 and 2.8.

4.4 Discussion

The 2D gravity model (Figure 4.4) shows the maximum depth-to-basement is approximately 3 km. The overall basin geometry suggested by the model is remarkably similar to the 2D MT models, differing primarily at the center of the modeled basin. The observed and modeled low resistivities could be explained by the presence of saline fluid in the pore space following Archie's Law [Archie, 1942] and thermal effects [Ussher *et al.*, 2000; Kulenkampff *et al.*, 2005; Milsch *et al.*, 2010], which both

increase the bulk electrical conductivity of the host rock. Forward modeling of a down hole resistivity log from well 81-7 Pavant Butte agrees with MT soundings recorded in the immediate vicinity which display apparent resistivity monotonically decreasing with depth. MT soundings recorded through the central part of the basin are also quite similar to those near well 81-7 Pavant Butte. Since the current data set does not reach the southern end of the basin completely, the southern extent of this interesting MT response is uncertain until the 2012 data have been fully analyzed. It appears that a 15 km wide area of the basin with sediment thickness > 2 km overlies the basement. These thick sediments constitute a thermal blanket that increases the temperature of the potential stratigraphic reservoir due to thermal conductivity effects [Allis *et al.*, 2011, 2012].

The high-resistivity structure in the MT models is interpreted to be basement marbleized Cambrian limestone and dolomite yielding depth-to-basement estimates of 1 to 2 km near the western and eastern margins. At the center of the model lines, there is no clear indication of the basement interface which could be due to the truncation of MT data at 10 seconds with the intent to minimize 3D effects. Thin high-resistivity layers near the surface are interpreted as thin basalt flows and are consistent with surface observations. The low-resistivity bodies are interpreted to be basin sediments and appear to extend to at least basement depth (approximately 3 km) as revealed by oil and gas wells. These conductors are interpreted to be clays near the surface and hot, saline fluids, or a combination thereof at depth. Since it is unlikely that there are extensive and thick clay layers deep in the basin (supported by well logs), it is proposed that hot, saline fluids and temperature effects are producing the low-resistivity structure at depth.

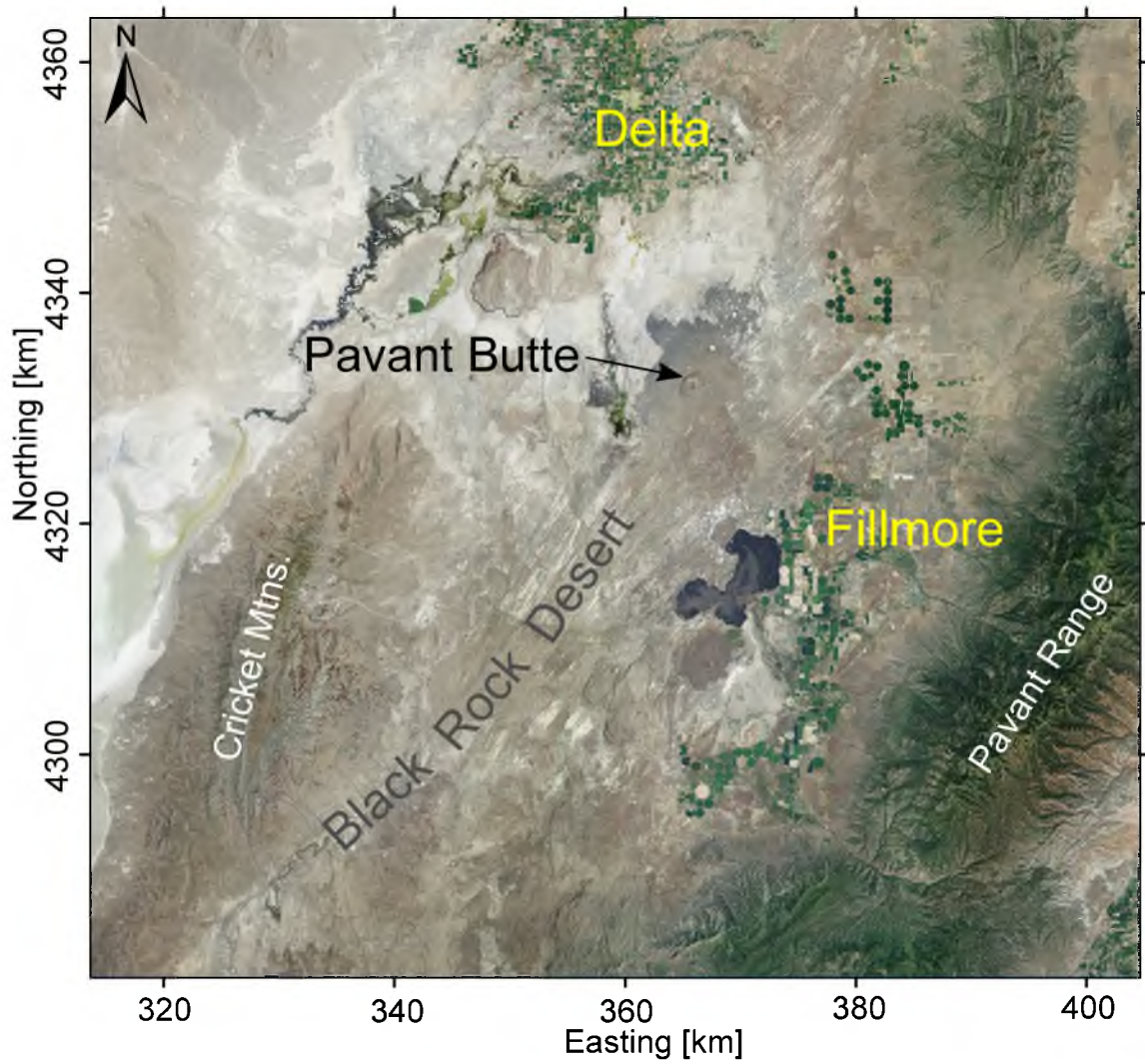


Figure 4.1. Pavant Butte field area showing the Black Rock Desert.

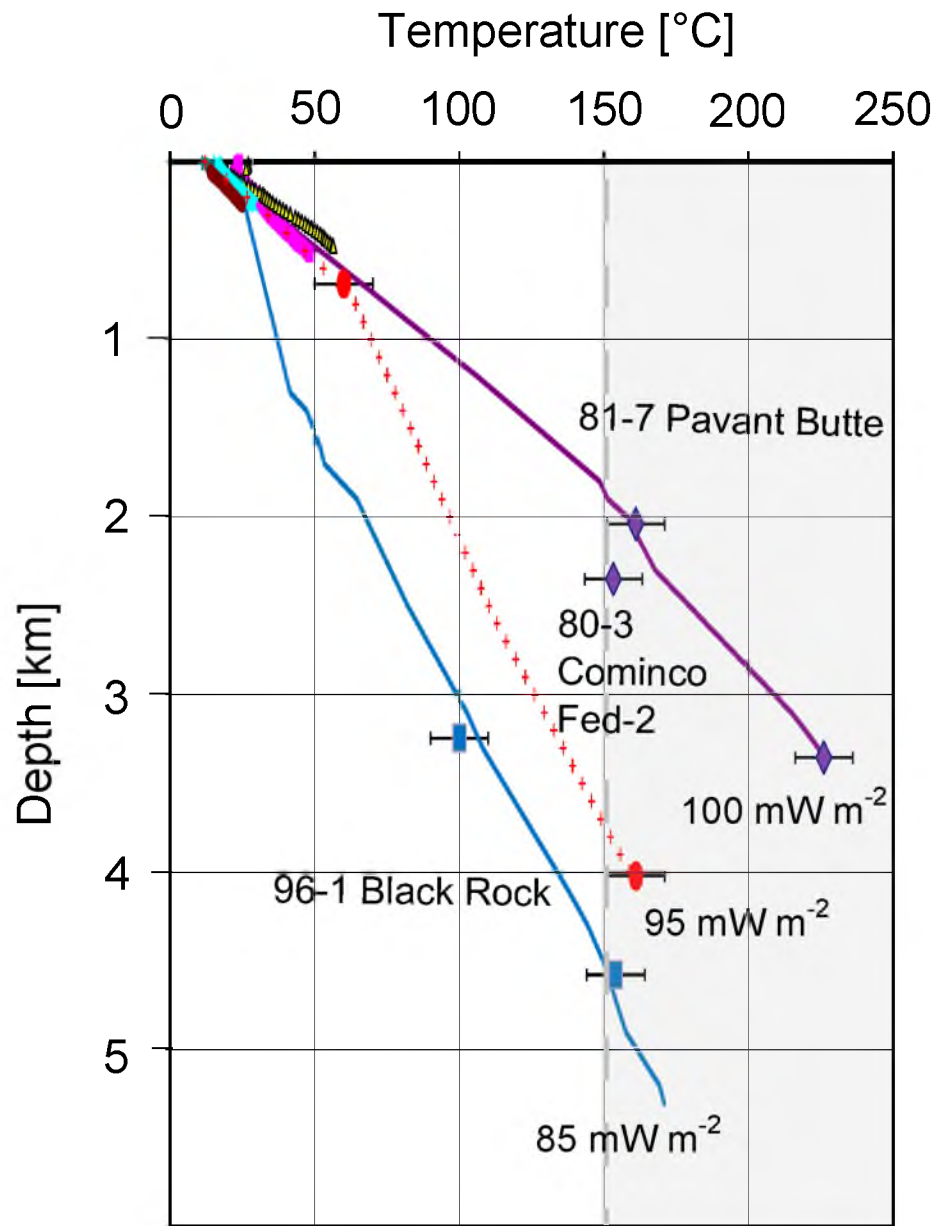


Figure 4.2. Thermal gradients in the Black Rock Desert for selected wells. Symbols show corrected bottom hole temperatures with error bars and heat-flow values are indicated. Vertical dashed line indicates ideal minimum temperature for geothermal targets. Modified from *Allis et al.* [2012].

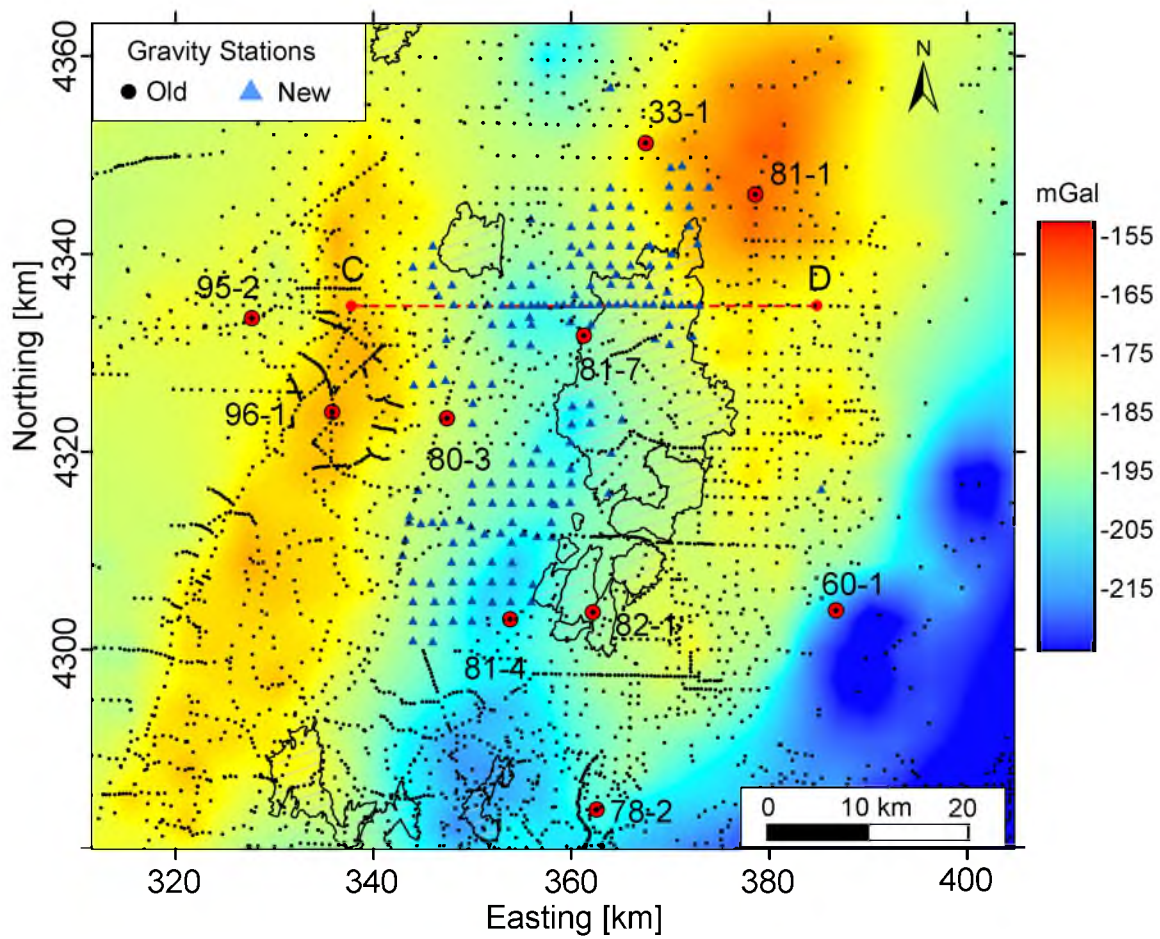


Figure 4.3. Complete Bouguer gravity anomaly map. Black hatched areas outline volcanic flows, red circles with black centers are deep exploration wells identified by well number. Red dashed line CD is gravity model transect.

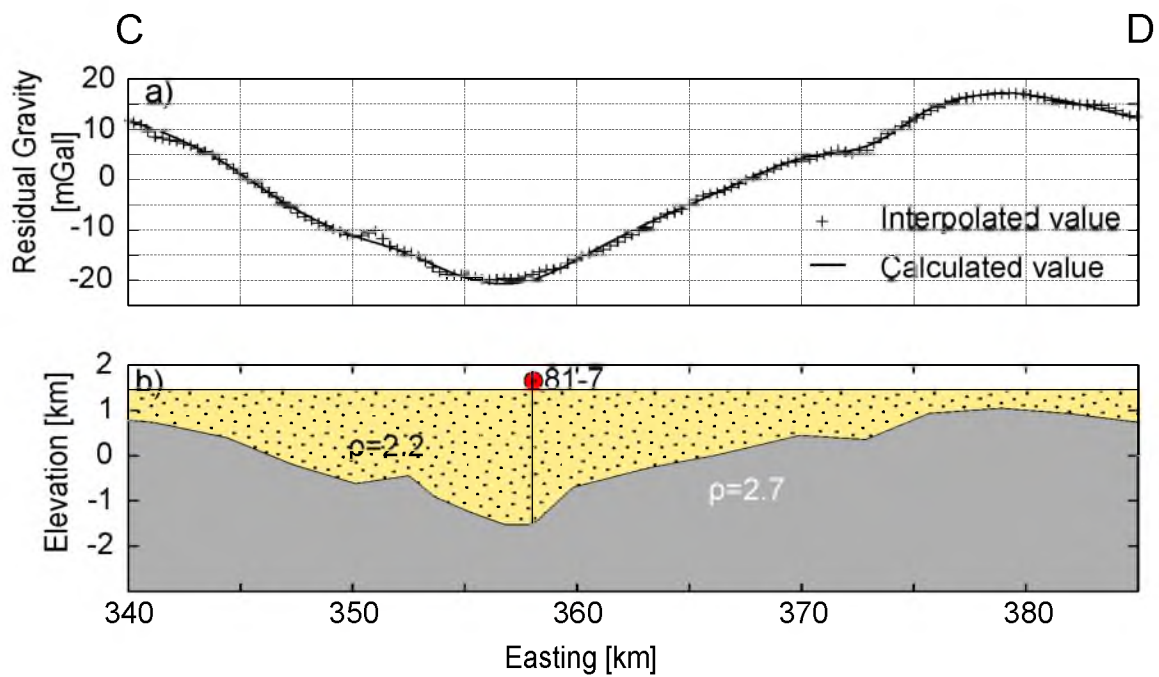


Figure 4.4. Residual gravity (a) and 2D gravity model (b) for transect CD (Figure 4.3). Light and dark colored layers represent sedimentary fill and basement rock respectively. Densities indicated are g cm⁻³. Pavant Butte well 81-7 indicated by red circle with black center.

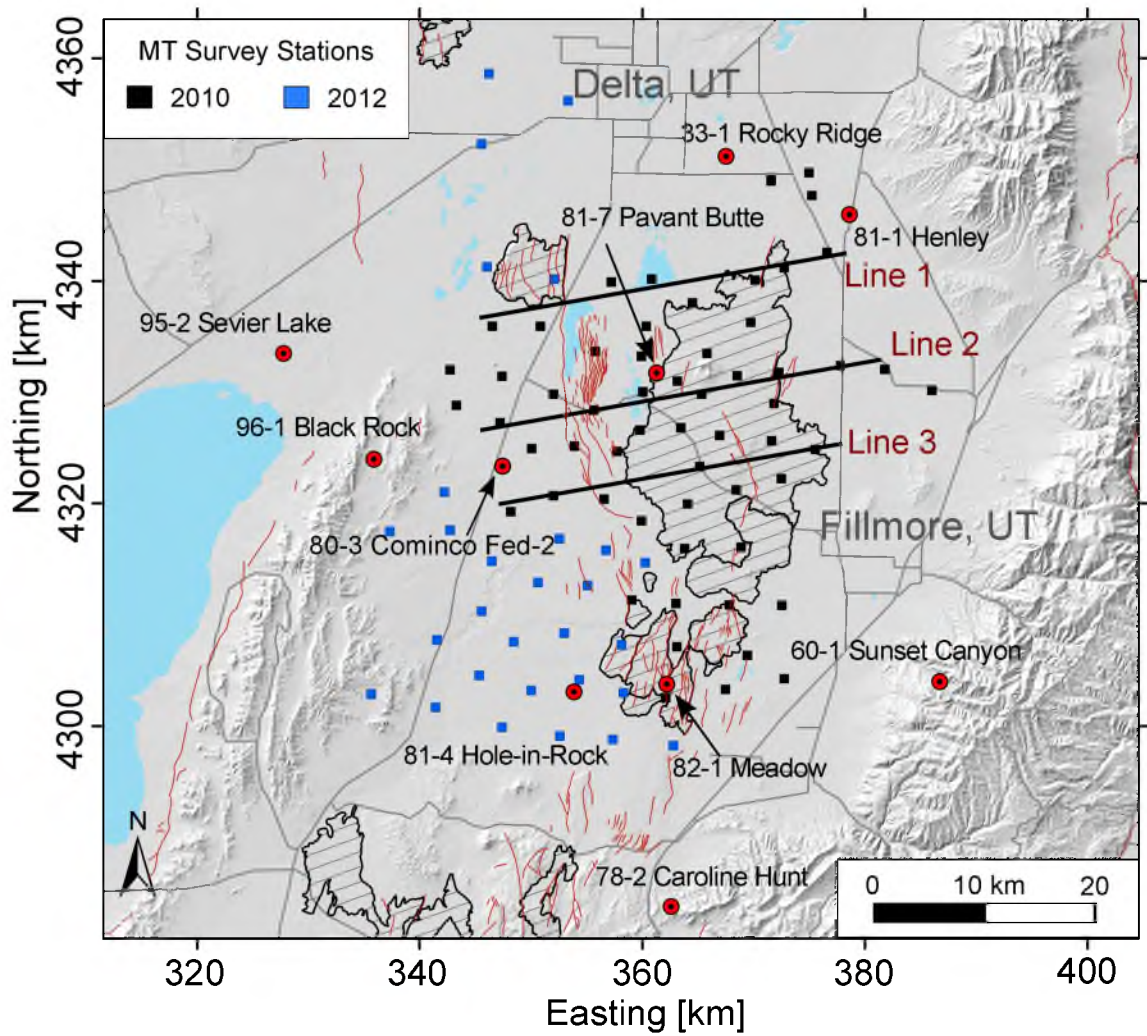


Figure 4.5. Map of Black Rock Desert and Pavant Butte MT survey area. Red Circles with black centers are deep exploration wells from Hintze and Davis (2003). Black hatched are volcanic flows, red lines denote Quaternary faults, bold black lines are MT 2D model transects, and light gray lines are local roadways.

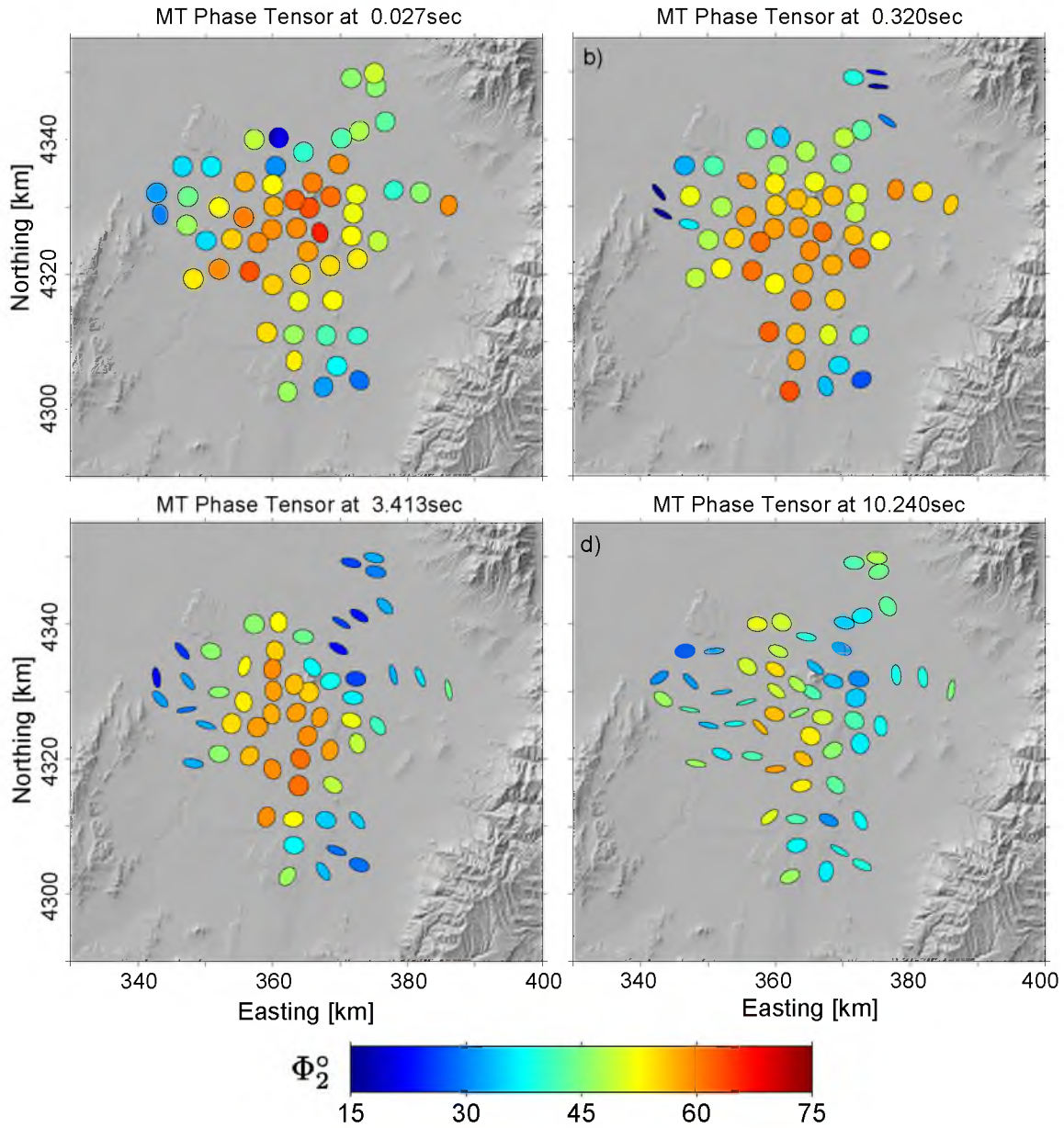


Figure 4.6. MT phase tensor ellipse maps for select periods (a,b,c,d) of the Pavant Butte MT survey. Phase tensors at shorter periods are circular, indicating 1D conditions and change to ellipses at longer periods, indicating 2D and 3D conditions. Phase tensor color is the geometric mean of the minimum and maximum phases and indicates the conductivity gradient of subsurface structure (i.e., $< 45^\circ$ more resistive and $> 45^\circ$ more conductive). Low-phase values appearing at the outer margins of the data are interpreted as detection of the high-resistivity basement rock. The low-resistivity of the basin sediments are reflected in the high-phase values observed in the central data.

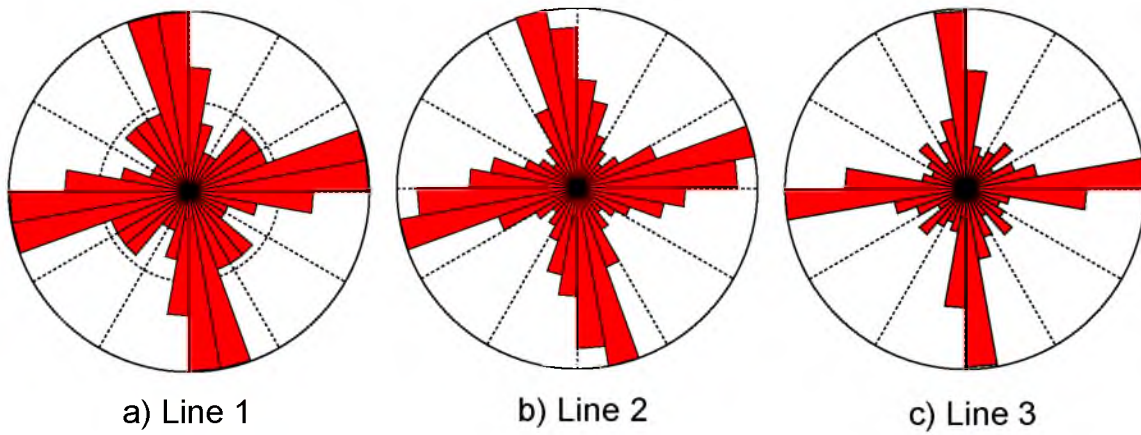


Figure 4.7. Strike directions of Pavant Butte MT transect lines (a,b,c). Directions are in geographic coordinates and computed from phase tensor parameters. A consistent trend of azimuth 80° (or 350°) is observed for all lines.

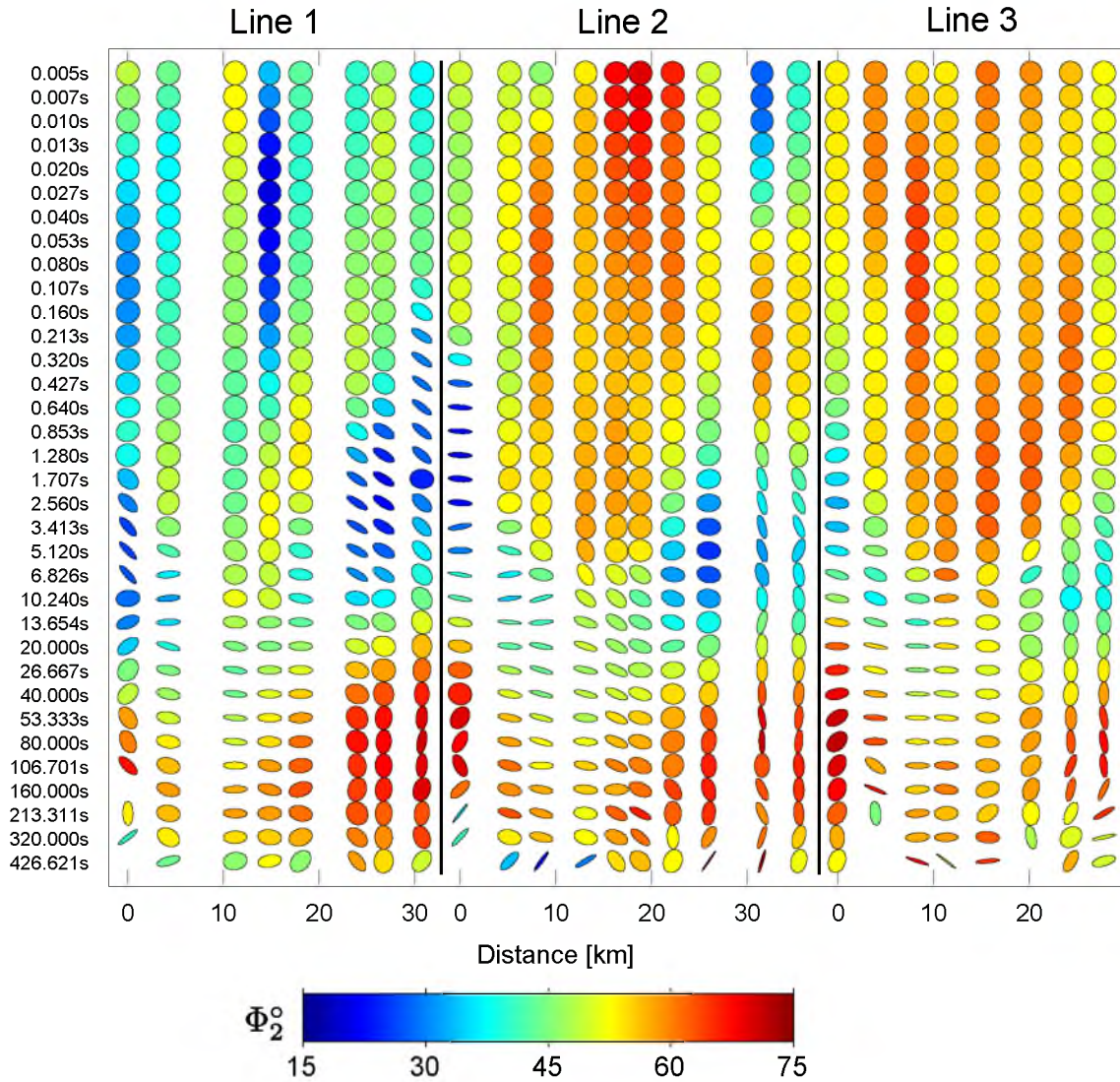


Figure 4.8. Phase tensor ellipses for Pavant Butte MT transects. Ellipses are arranged by transect line and period. Phase tensors at shorter periods are circular, indicating 1D conditions and change to ellipses at longer periods, indicating 2D and 3D conditions. Phase tensor color is the geometric mean of the minimum and maximum phases and indicates the conductivity gradient of subsurface structure (i.e., $< 45^\circ$ more resistive and $> 45^\circ$ more conductive). High phase values in lines 2 and 3 indicate a transition into a more conductive structure in the central part of the basin. Resistive basement is reached in the data at periods after 2 seconds at the ends of each line.

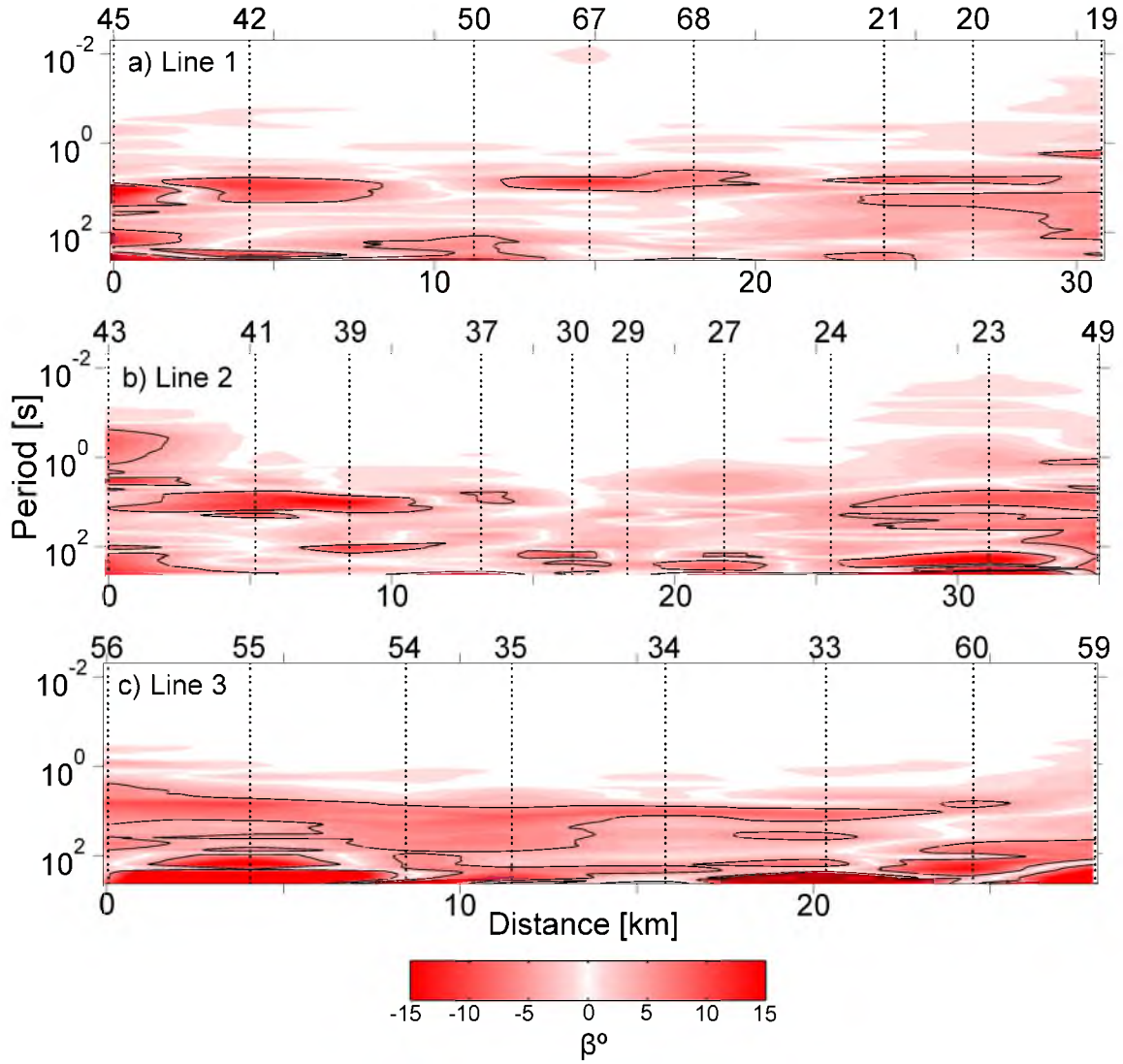


Figure 4.9. Dimensionality for MT transects (a,b,c) of Pavant Butte. Skew angle is a phase tensor parameter that assists in distinguishing 2D and 3D data. Contours shown are for $-5/+5$ skew values; outside of this range, the data are most likely 3D. For lines 1 and 2, the data are considered mostly 2D with exception of a few outliers. Line 3 appears to be 2D until around a 10-second period where the skew indicates it is 3D.

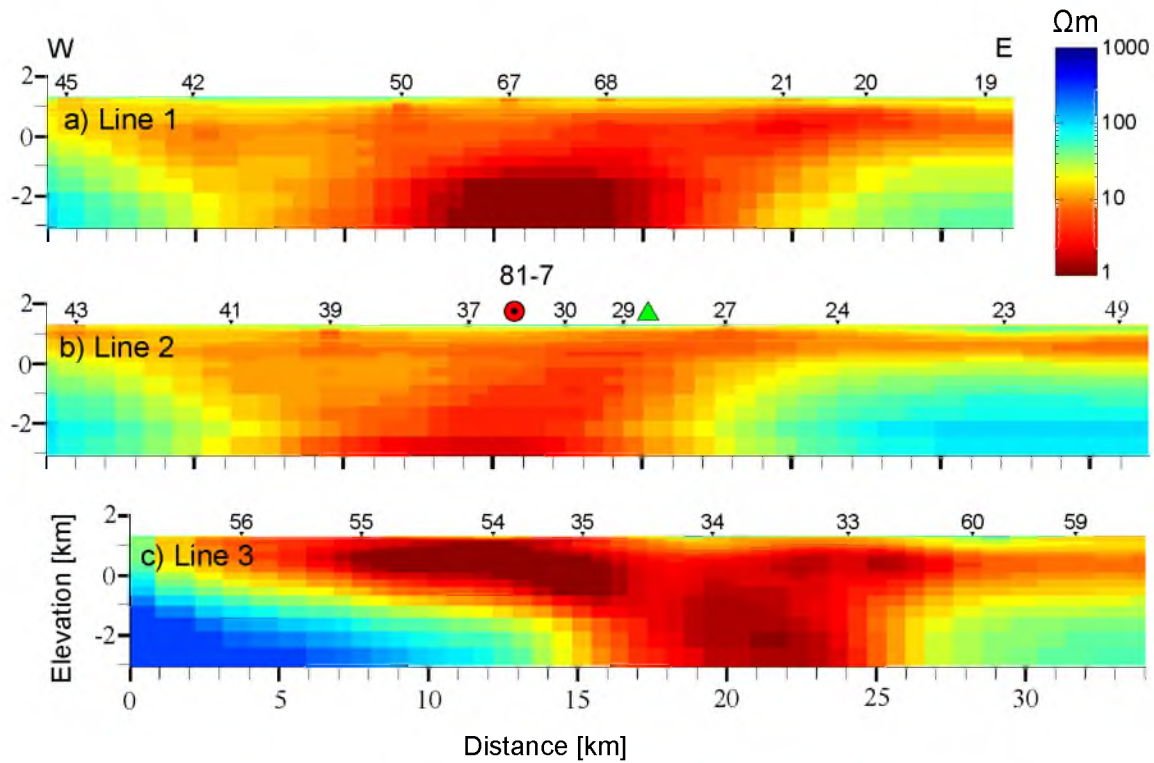


Figure 4.10. Two-dimensional MT resistivity models for Pavant Butte. Profile locations are shown in Figure 4.4. MT stations are indicated by black, inverted triangles with station numbers shown. Green triangle is Pavant Butte and red circle with black center is Pavant Butte well 81-7. Models were created using the 2D inversion program of *Wannamaker et al.* [1987] with TM mode and induction vector data. Final nRMSE values are 2.8, 1.8, 2.4 for each line, respectively.

CHAPTER 5

THERMO HOT SPRINGS

5.1 Introduction

Thermo Hot Springs (Figure 5.1), an existing 10 MWe geothermal resource in southern Utah, is poorly understood with little constraint on subsurface extent and capacity. The existing geothermal plant (Hatch plant, shown in Figure 5.1) uses 140°C fluids extracted from the subsurface in a binary heat exchanger system to produce electricity. *Sawer* [1977] proposed that the location of the hot springs is controlled by the intersection of an east-west and a north-south trending fault inferred from gravity models. In an effort to expand geothermal production, the subsurface extent and source of the system is being explored by gravity and MT surveys. With the addition of borehole data, thermal gradient wells, and water chemistry we aim to constrain the extent of the geothermal system, identify its source, and quantify its total production potential.

5.2 Gravity

5.2.1 Survey and Modeling

Gravity measurements in the vicinity of Thermo Hot Springs were previously reported by *Sawer* [1977]. A total of 108 gravity stations were measured during a 2-week period in the summer of 2010 (Figure 5.2). A station spacing of approximately 1 to 2 km along existing roads was used in order to achieve better coverage in areas adjacent to MT observations.

Two simple 2D gravity models were developed using layers to represent the local geology. Transect EF (Figures 5.2 and 5.3) was modeled using two layers with the focus of constraining sediment thickness in the southwestern area. The layer densities of 2.2 and 2.7 g cm⁻³ for sediments and basement rock, respectively, were based on

average values for the appropriate lithology from regional geology reports and logs of nearby wells [Rowley, 1978; Nash and Jones, 2012]. Transect GH (Figures 5.2 and 5.4) was modeled in collaboration with Anderson [2012] and focuses on mapping the buried structure at the Thermo geothermal field and nearby areas. A two-layer gravity model was also used here since the density contrasts between lithologic units were not significant enough to justify multiple layers other than an upper basin-fill unit and a lower bedrock unit. Densities of 2.4 and 2.7 gm cm⁻³ are used for basin-fill and bedrock, respectively, and the gravity model is constrained using lithologic logs of wells located in the geothermal field [Nash and Jones, 2012].

5.2.2 Results

The Thermo study area appears to have a more complicated structural/density character in the subsurface than that of a typical Basin and Range setting. The complete Bouguer gravity anomaly (Figure 5.2), displays a complex gravity field with a number of small and large anomaly features. The most striking feature is a gravity low of approximately 20 mGal along the western edge of the basin extending more than 20 km southward from Blue Mountain. There are also localized gravity highs and lows of approximately 5 to 10 mGal amplitude observed over the basin fill due east of the hot springs. These localized gravity highs and lows are observed where there is somewhat descent data coverage and imply that there are local structural features or density heterogeneities existing near the surface.

The 2D gravity model of transect EF (Figure 5.3) fits an asymmetrical basin shape with eastward-stepping faults in bedrock and a maximum sediment thickness of 2 km. There do not appear to be any faults in the bedrock along the gently dipping, eastern side of the transect though faults have been mapped at the surface and in the nearest volcanic vent, Blue Knoll, in the work of Rowley [1978]. Transect GH, shown in Figure 5.4, shows a minimum sediment thickness of 200 m and a maximum thickness of 1.2 km. The structural interpretation of transect GH, by Anderson [2012], was based on field observations of surface fault traces and well logs

and shows a series of low-angle normal faults and multiple sets of horst and graben structures.

5.3 Magnetotellurics

5.3.1 Survey and Analysis

A total of 90 magnetotelluric (MT) soundings spread over an area of approximately 600 km², with an average station spacing of 2 to 3 km (Figure 5.5), were completed during the summer of 2010 with occupation times of 12 to 24 hours. Stations were distributed throughout the area surrounding the hot springs including a wide birth (1.6 km) given to the local railway and electric transmission lines. MT phase tensor maps (Figure 5.6) are plotted for select periods ranging from 0.01 to 20 seconds for initial data analysis. At the shortest period (0.01 s, Figure 5.6a), widespread 1D conditions (circular shape) are observed but quickly transition to 2D (elliptical shape) afterwards. The resistive basement is detected first by the data in the northwest by 0.32 s (Figure 5.6c) which are followed by data in the northeast in subsequent periods. A relatively conductive structure is detected in the basin to the southeast in Figures 5.6b–5.6c until around 1.28–2.56 s (Figures 5.6e and 5.6f) where phase indicates the resistive basement is sensed.

Careful observation of the data reveals that the preferred orientation of the MT phase tensor slowly rotates with period. This rotation is more pronounced in the data located in the eastern and northeastern study area. Phase tensors at earlier periods are oriented at northeast direction and smoothly rotate to an eastward direction with increasing period. If the data were truly 2D, the strike direction will have some inherent variation due to measurement errors or noise; however, it would not change in such a uniform manner. This is indicating that the data are 3D which implies the subsurface structure is 3D since the strike direction is not constant (within measurement error).

The analysis of the phase tensor skew supports the 3D dimensionality attributed to the data which was inferred from the directionality (discussed above). Skew angles greater than even the modest condition of $\beta \leq 3^\circ$ are widespread for periods larger than 0.32 s. This means there is very little data remaining to invert that could be

considered 2D based on the skew criteria only. When we consider directionality, it is clear that the data are 3D and require a 3D treatment since the 2D assumption for 2D inversion would not be valid.

5.4 Discussion

Complete Bouguer anomaly shows a prominent north-south regional trend of 10 to 15 mGal amplitude which is interpreted as a large Basin-and-Range normal fault. Northeast of the hot springs, there is an east-west trending gravity low of 4 mGal amplitude which is interpreted as a fault with down throw to the north. These two trends intersect adjacent to the hot spring, and are interpreted to be the structural control of the fluid flow [Sawer, 1977]. Results from 2D inversion models of gravity profiles provide depth-to-basement values as shallow as 200 m near the hot spring and as deep as 2 km in the southwest of the study area. We believe that the low resistivities observed in the southwest indicate the existence of hot fluids and/or clay rich sediments at a thickness of more than 1.5 km overlying hot, saturated basement rock. A deep, stratigraphically-hosted geothermal system could be present in the southwest and may be connected to the hot springs through a north-trending, deeply-penetrating fracture zone.

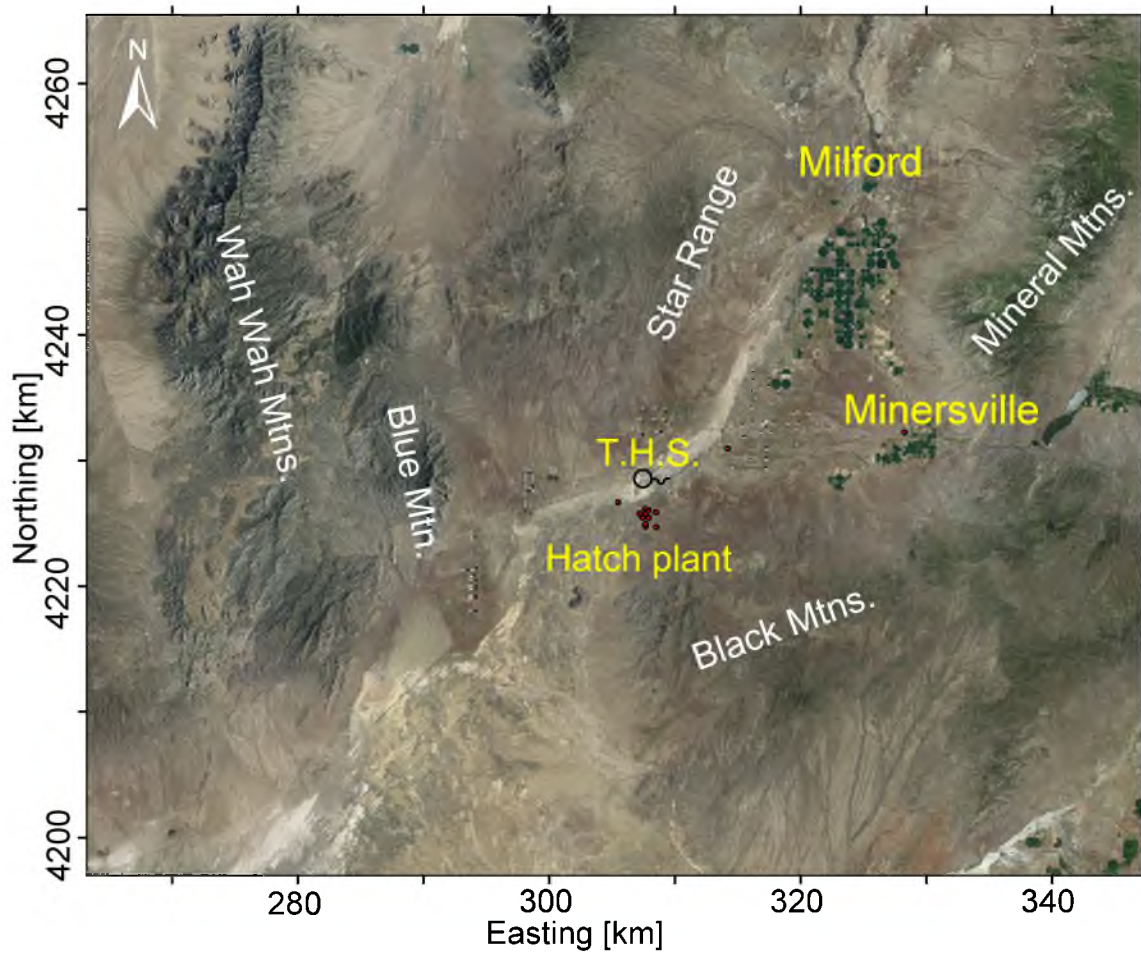


Figure 5.1. Map of Thermo Hot Springs study area. Red dots indicate locations of local wells and Thermo Hot Springs is denoted by a black spring symbol.

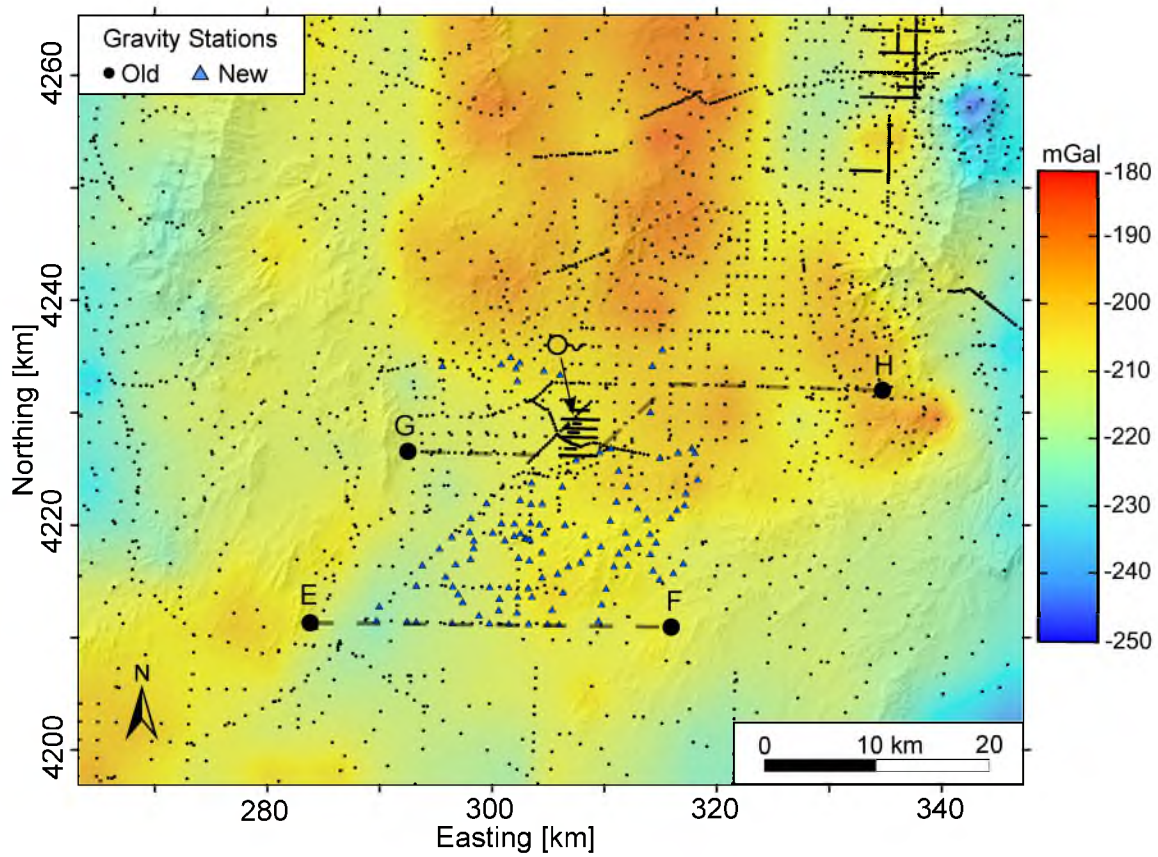


Figure 5.2. Complete Bouguer gravity anomaly map of the Thermo Hot Springs study area. Dashed lines indicate gravity model transects EF and GH. The location of Thermo Hot Springs is indicated by a black spring symbol.

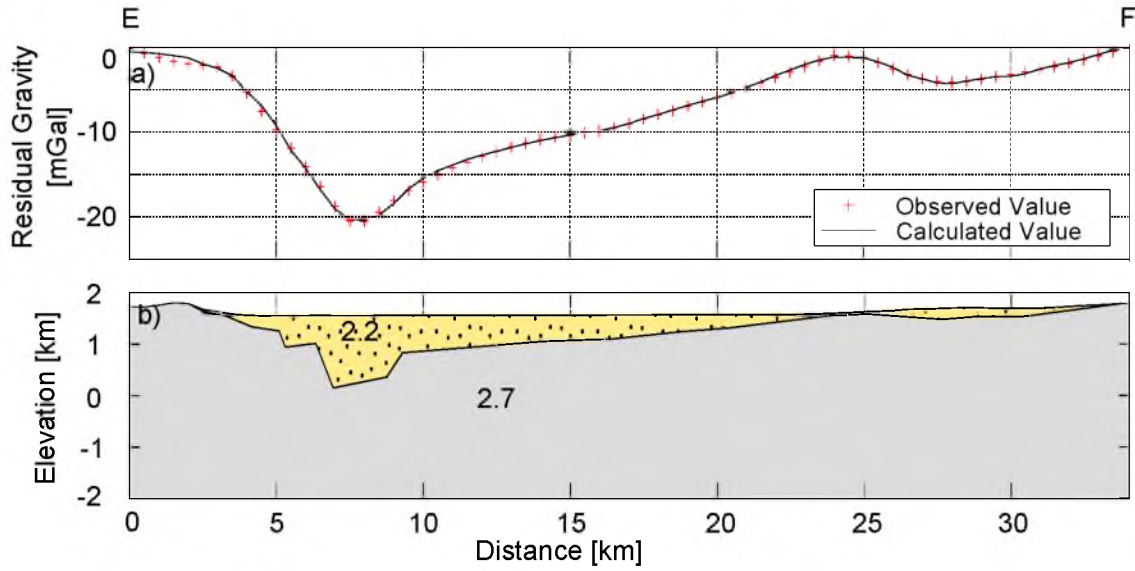


Figure 5.3. Residual gravity (a) and 2D gravity model (b) for transect EF. Yellow and gray colored lithologies are the basin fill and basement rock, respectively. Densities are given in units of g cm^{-3} .

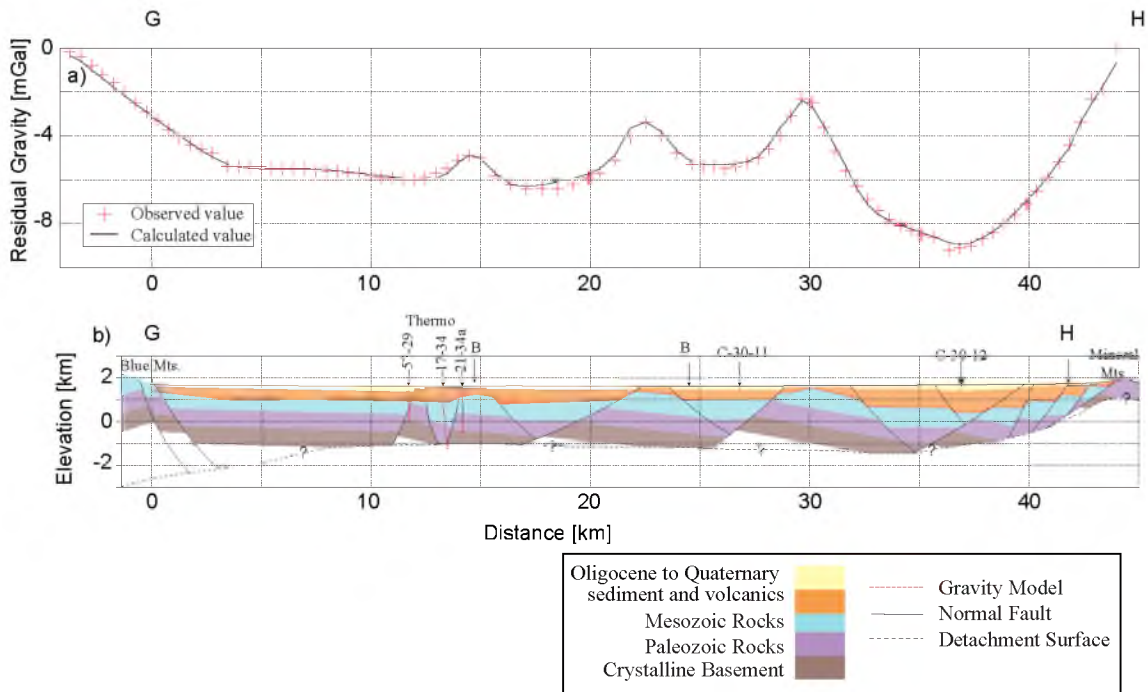


Figure 5.4. Residual gravity (a) and 2D gravity model (b) with structural interpretation for transect GH. Model control is based on wells indicated by solid red lines and bends in transect line are denoted by B. Modified from *Anderson [2012]*.

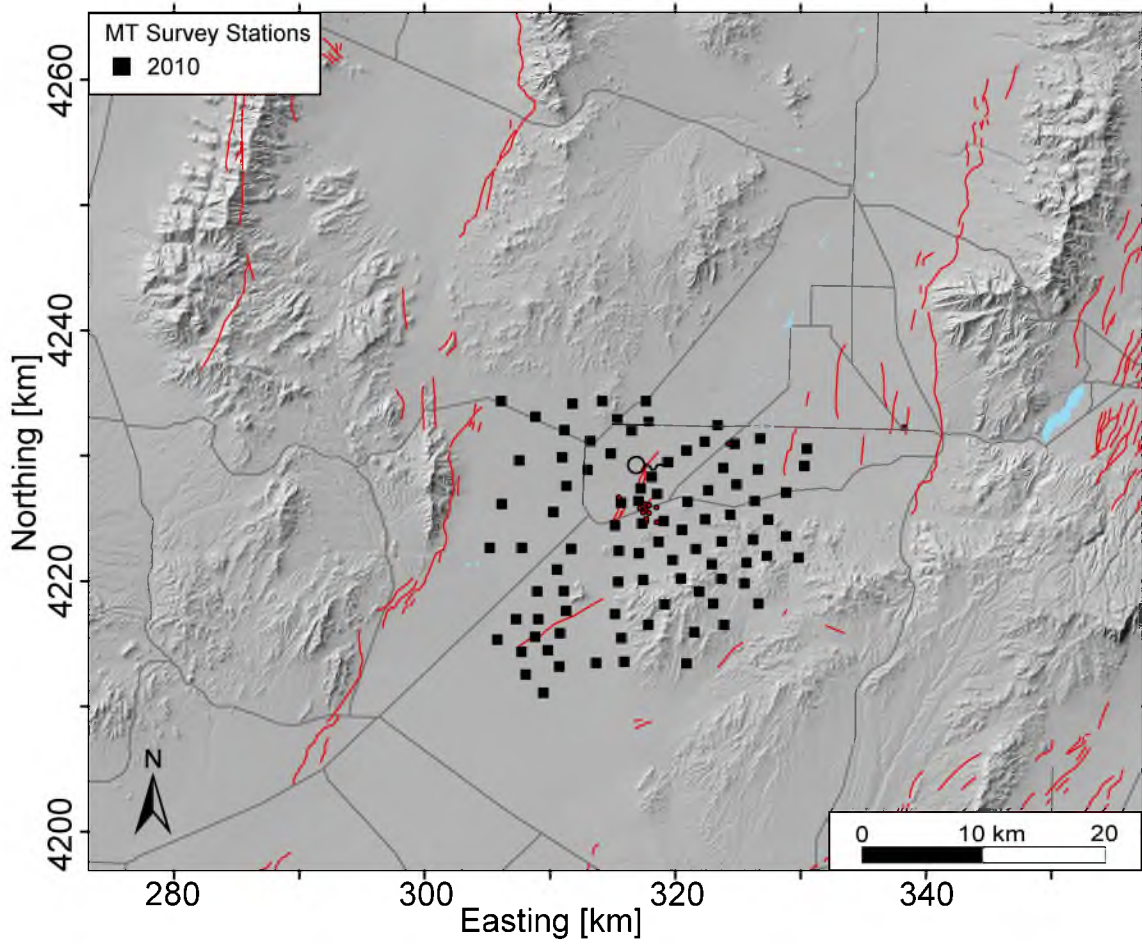


Figure 5.5. Thermo Hot Springs MT survey area. Solid black squares show MT stations, red lines denote Quaternary faults, and gray lines are local road ways. Thermo Hot Springs indicated by black spring symbol and red dots show location of local wells.

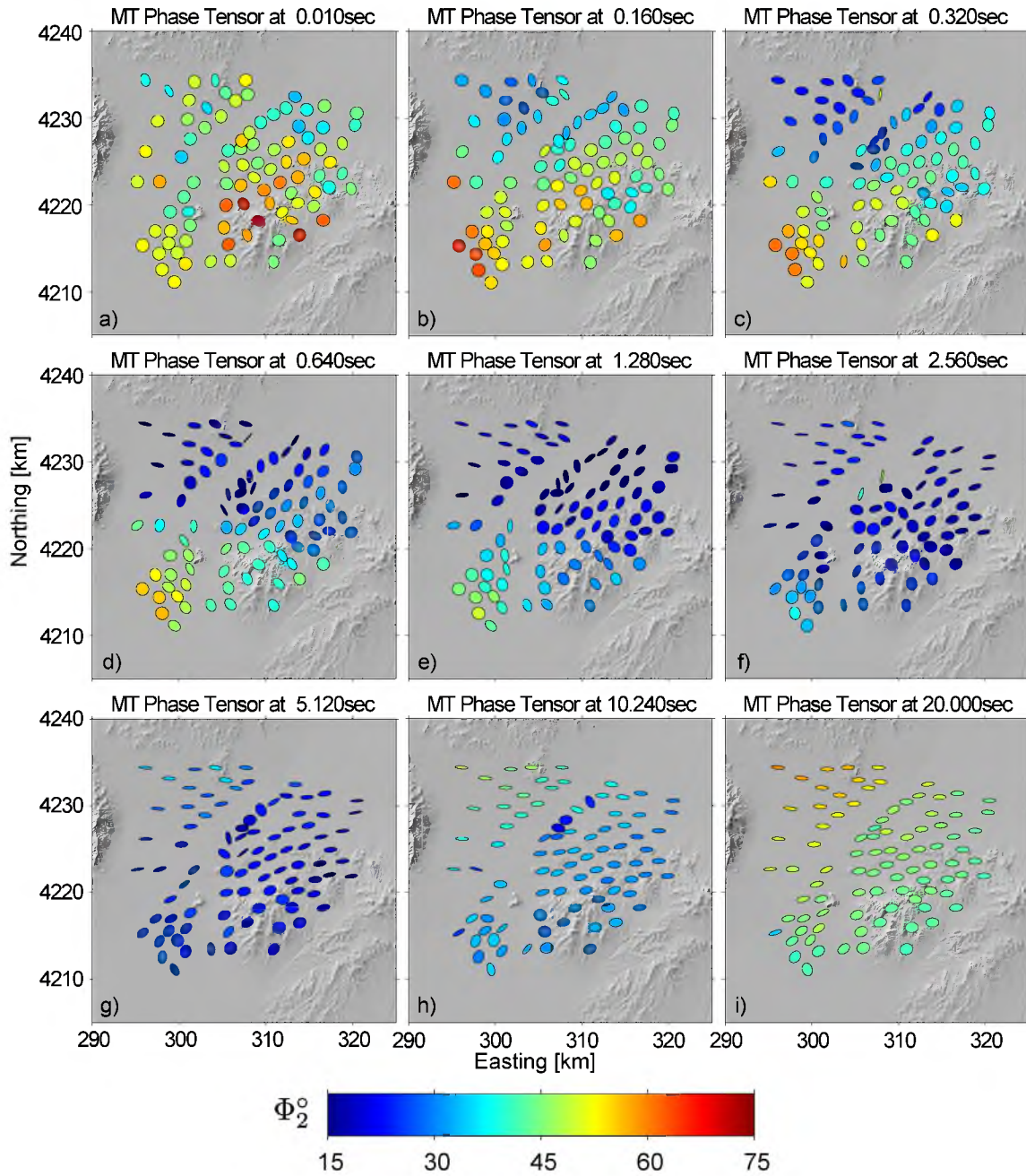


Figure 5.6. MT phase tensor ellipse maps for select periods (a-i) of the Thermo Hot Springs MT survey. Phase tensors at shorter periods are circular, indicating 1D conditions and change to ellipses at longer periods, indicating 2D and 3D conditions. Phase tensor color is the geometric mean of the minimum and maximum phases and indicates that conductivity gradient of subsurface structure (i.e., $< 45^\circ$ more resistive and $< 45^\circ$ more conductive). Maps show widespread 1D conditions in the shortest period, but quickly transition to 2D afterwards. Resistive basement is detected first in the northwest followed by the northeast in longer periods. A relatively conductive structure is detected in the southwest at shorter periods.

CHAPTER 6

SUMMARY AND CONCLUSIONS

Based on the above findings we conclude the following:

1. Modeling of the deep structure interpreted as basement has good agreement between both the MT and gravity data sets for the Crater Bench study area. A geothermal system with a major volcanic heat component does not appear to be represented by the MT modeling though it may still be a minor factor. It is proposed that the horst block is a conduit for the flow of fluids from a much deeper, hydrothermal system such as those suggested by *Allis et al.* [2011] should be explored further.
2. Two-dimensional models of the Black Rock Desert of western Utah show good agreement between both the MT and gravity data sets for the Pavant Butte study area. Thick sediments overlying the basement provide excellent conditions for the existence of stratigraphic reservoirs at depth. High temperatures and anomalous heat flow observed at Pavant Butte could be isolated from the rest of the basin and perhaps directly related to Quaternary faults to the east and west which could provide flow paths to the surface for hot fluids, resulting in convective heat flow conditions rather than conductive.
3. Structural control of the natural hot springs located at Thermo are believed to be due to the intersection of orthogonal normal faults. The fluids used in production at the geothermal plant are a relatively low temperature ($<160^{\circ}\text{C}$) and appear to be connate waters [*J. Moore, personal comm.*, 2012] which implies that these fluids are regional fluids and not from a local heat source. It is thought that the geothermal fluids originate in the southwest basin and connect to the hot springs system through north-trending, deeply-penetrating fracture zone. To gain better perspective of this geothermal system and its

structural control it is recommended that both the gravity and MT data are modeled using 3D techniques.

REFERENCES

- Allis, R. G., J. Moore, R. E. Blackett, M. Gwynn, S. Kirby, and D. Sprinkel (2011), The potential for basin-centered geothermal resources in the Great Basin, *Geothermal Resources Council Transactions*, *35*, 683–688.
- Allis, R. G., R. E. Blackett, M. Gwynn, C. L. Hardwick, J. M. C. Morgan, D. Schelling, and D. Sprinkel (2012), Stratigraphic reservoirs in the Great Basin - the bridge to development of enhanced geothermal systems in the U.S., *Geothermal Resources Council Transactions*, *36*, 351–357.
- Anderson, W. V. (2012), Implications of thrust and detachment faulting for the structural geology of the Thermo Hot Springs KGRA, Beaver county, Utah, Master's thesis, University of Utah.
- Archie, G. E. (1942), The electric resistivity log as an aid in determining some reservoir characteristics, *Transactions AIME*, *146*(1), 54–62.
- Bibby, H. M., T. G. Caldwell, and C. Brown (2005), Determinable and non-determinable parameters of galvanic distortion in magnetotellurics, *Geophys. J. Int.*, *163*, 327–344.
- Blackett, R. E. (2007), Review of selected geothermal areas in southwestern Utah, *Geothermal Resources Council Transactions*, *31*, 111–116.
- Booker, J. (2012), The magnetotelluric phase tensor: a critical review, 21st Electromagnetic Induction Workshop, Darwin, N.T., Australia.
- Brumbaugh, W. D. (1978), Gravity survey of the Cove Fort-Sulfurdale KGRA and the north Mineral Mountains area, Millard and Beaver counties, Utah, Master's thesis, University of Utah, 131p.
- Bujakowski, W., A. Barbacki, B. Czerwinska, L. Pajak, M. Pussak, M. Stefaniuk, and Z. Trzesniowski (2010), Integrated seismic and magnetotelluric exploration of the Skierniewice, Poland, geothermal test site, *Geothermics*, *39*(1), 78–93.
- Cagniard, L. (1953), Basic theory of the magneto-telluric method of geophysical prospecting, *Geophysics*, *18*, 605–635.
- Caldwell, T. G., H. M. Bibby, and C. Brown (2004), The magnetotelluric phase tensor, *Geophys. J. Int.*, *158*, 457–469.
- Carter, J. A. (1978), Regional gravity and aeromagnetic surveys of the Mineral Mountains and vicinity, Millard and Beaver counties, Utah, Master's thesis, University of Utah, 178p.

- Cordell, L. (1992), A scattered equivalent-source method for interpolation and gridding of potential-field data in three dimensions, *Geophysics*, 57(4), 629–636.
- Crebs, T. J. (1976), Gravity and ground magnetic surveys of the central Mineral Mountains, Utah, Master's thesis, University of Utah, 129p.
- de Lugao, P. P., and P. E. Wannamaker (1996), Calculating the two-dimensional magnetotelluric Jacobian in finite elements using reciprocity, *Geophys. J. Int.*, 127, 806–810.
- Garg, S. K., J. W. Pritchett, P. E. Wannamaker, and J. Combs (2007), Characterization of geothermal reservoirs with electrical surveys: Beowawe geothermal field, *Geothermics*, 36, 487–517.
- Gettings, P. (2013), Ph.D. thesis, University of Utah.
- Gettings, P., D. S. Chapman, and R. Allis (2008), Techniques, analysis, and noise in a Salt Lake Valley 4D gravity experiment, *Geophysics*, 73(6), WA71–WA82.
- Gilbert, G. K. (1890), Lake Bonneville, *U.S. Geological Survey Monograph*, 1, 332–335.
- Hammer, S. (1939), Terrain corrections for gravimeter stations, *Geophysics*, 4, 184–194.
- Heise, W., T. G. Caldwell, H. M. Bibby, and C. Brown (2006), Anisotropy and phase splits in magnetotellurics, *Physics of the Earth and Planetary Interiors*, 158, 107–121.
- Hintz, A. R. (2008), Physical volcanology and hazard analysis of a young monogenetic volcanic field: Black Rock Desert, Utah, Master's thesis, University of South Florida.
- Hintze, L. F., and F. D. Davis (2003), Geology of Millard county, Utah, *Bulletin* 133, Utah Geological Survey.
- Hinze, W. J., et al. (2005), New standards for reducing gravity data: The North American gravity database, *Geophysics*, 70(4), J25–J32.
- Jiracek, G. R. (1990), Near-surface and topographic distortions in electromagnetic induction, *Surv. Geophys*, 11, 163–203.
- Johnson, E. H. (1975), Resistivity and induced polarization survey of a basalt flow in a geothermal environment, western Utah, Master's thesis, University of Utah, 69p.
- Johnston, J. M., L. Pellerin, and G. W. Hohmann (1992), Evaluation of electromagnetic methods for geothermal reservoir detection, *Geothermal Resources Council Transaction*, 16, 241–245.

- Kulenkampff, J., E. Spangenberg, O. G. Flovenz, S. Raab, and E. Huenges (2005), Petrophysical parameters of rocks saturated with liquid water at high temperature geothermal reservoir conditions, World Geothermal Congress Proceedings, Antalya, Turkey.
- LaFehr, T. R. (1991), An exact solution for the gravity curvature (Bullard B) correction, *Geophysics*, 56, 1179–1184.
- Milsch, H., E. Spangenberg, S. Raab, A. Schepers, G. Blocher, D. Bruhn, L. H. Kristinsdottir, O. G. Flovenz, and E. Huenges (2010), Effects of pressure, temperature, fluid-rock interactions, and phase changes on the physical properties of geothermal reservoir rocks: the experimental perspective, World Geothermal Congress Proceedings, Bali, Indonesia.
- Moritz, H. (1980), Geodetic Reference System 1980, *Bulletin Geodesique*, 54, 395–405.
- Mundorff, J. C. (1970), Major thermal springs of Utah, *Water Resources Bulletin* 13, Utah Geological and Mineral Survey, 60p.
- Nash, G. D., and C. Jones (2012), Thermo geothermal drilling program rock reports: wells 11-34, 24-34, 13-34a, 58-34, 52-34, 21a-34, 63-33, 74-34, and 17-34, Energy and Geoscience Institute, University of Utah, unpublished report, 56p.
- Nash, W. P., C. Turley, J. Peterson, and F. H. Brown (1978), Volcanism and the regional assessment of geothermal potential in west-central Utah, *Geothermal Resources Council Transactions*, 2, 475–477.
- Palacky, G. J. (1988), Resistivity characteristics of geologic targets, in *Electromagnetic methods in applied geophysics*, edited by M. N. Nabighan, 1, pp. 53–130, Soc. of Expl. Geophys.
- Parkinson, W. D. (1962), The influence of continents and oceans on geomagnetic variations, *Geophys. J. R. Astron. Soc.*, 6, 441–449.
- Peterson, J. B. (1979), A petrologic study of the Fumarole Butte volcanic complex, Utah, Master's thesis, University of Utah, 63p.
- Rowley, P. D. (1978), Geologic map of the Thermo 15-minute quadrangle, Beaver and Iron counties, Utah, *Map GQ-1493*, U.S. Geological Survey.
- Rush, E. F. (1983), Reconnaissance of the hydrothermal resources of Utah, *Professional Paper 1044-H*, U.S. Geological Survey, 44p.
- Saltus, R. W., and R. J. Blakely (2011), Unique geologic insights from "non-unique" gravity and magnetic interpretation, *Geological Society of America Today*, 21(12), 4–11.
- Sawer, R. F. (1977), Gravity and ground magnetic surveys of the Thermo Hot Springs KGRA region Beaver county, Utah, Master's thesis, University of Utah, 142p.

- Smith, T. B. (1974), Gravity study of the Fumarole Butte area, Juab and Millard counties, Utah, Master's thesis, University of Utah, 58p.
- Tarantola, A. (1987), *Inverse problem theory*, Elsevier, New York, 513p.
- Thangsuphanich, I. (1976), Regional gravity survey of the southern Mineral Mountains, Beaver county, Utah, Master's thesis, University of Utah, 38p.
- Tikhonov, A. N. (1950), On determining electrical characteristics of the deep layers of the Earth's crust, *Dokl. Akad. Nauk SSSR*, 73, 295–297.
- Ussher, G., C. Harvey, R. Johnstone, and E. Anderson (2000), Understanding the resistivities observed in geothermal systems, World Geothermal Congress Proceedings, Kyushu-Tohoku.
- Vozoff, K. (1991), The magnetotelluric method, in *Electromagnetic methods in applied geophysics*, edited by M. N. Nabighian, 2B, pp. 641–711, Soc. Expl. Geophys., Tulsa, Oklahoma.
- Wannamaker, P. E. (1999), Affordable magnetotellurics: interpretation in natural environments, in *Three-dimensional electromagnetics, Geophysical Development Series*, edited by M. Oristaglio and B. Spies, 7, pp. 349–374, Soc. of Expl. Geophys., Tulsa, Oklahoma.
- Wannamaker, P. E., J. A. S. L., and Rijo (1987), A stable finite-element solution for two-dimensional magnetotelluric modeling, *Geophys. J. R. Astron. Soc.*, 88, 277–296.
- Wannamaker, P. E., W. M. Doerner, and D. P. Hasterok (2006), Cryptic faulting and multi-scale geothermal fluid connections in the Dixie Valley-Central Nevada seismic belt area; implications from MT resistivity surveying, Stanford, California.
- Wannamaker, P. E., D. P. Hasterok, J. M. Johnston, J. A. Stodt, D. B. Hall, T. L. Sodergren, L. Pellerin, V. M. W. M. Doerner, and M. J. Unsworth (2008), Lithospheric dismemberment and magmatic processes of the Great Basin-Colorado Plateau transition, Utah, implied from magnetotellurics, *Geochemistry, Geophysics, Geosystems*, 9, Q05019, doi:10.1029/ 2007GC001886.
- Webring, M. W. (1985), SAKI—a Fortran program for generalized linear inversion of gravity and magnetic profiles, *Open-File Report 85-122*, U.S. Geological Survey, 104p.